Bioactive Materials 34 (2024) 164–180

Contents lists available at ScienceDirect

Bioactive Materials

journal homepage: www.keaipublishing.com/en/journals/bioactive-materials

# Photonic control of ligand nanospacing in self-assembly regulates stem cell fate

Sungkyu Lee [a,1], Jounghyun Yoo [b,1], Gunhyu Bae [a], Ramar Thangam [a], Jeongyun Heo [b], Jung Yeon Park [c], Honghwan Choi [b,c], Chowon Kim [a], Jusung An [d], Jungryun Kim [d], Kwang Rok Mun [e], Seungyong Shin [e], Kunyu Zhang [f], Pengchao Zhao [f], Yuri Kim [a], Nayeon Kang [a], Seong-Beom Han [c], Dahee Kim [a], Jiwon Yoon [b], Misun Kang [e], Jihwan Kim [b,c], Letao Yang [g], Solmaz Karamikamkar [h], Jinjoo Kim [h], Yangzhi Zhu [h], Alireza Hassani Najafabadi [h], Guosheng Song [i], Dong-Hwee Kim [c], Ki-Bum Lee [g], Soong Ju Oh [a], Hyun-Do Jung [j,s], Hyun-Cheol Song [k,l], Woo Young Jang [m], Liming Bian [f], Zhiqin Chu [n], Juyoung Yoon [o], Jong Seung Kim [d], Yu Shrike Zhang [p], Yongju Kim [c], Ho Seong Jang [e,q,*], Sehoon Kim [b,c,**], Heemin Kang [a,r,***]

[a] Department of Materials Science and Engineering, Korea University, Seoul, 02841, Republic of Korea
[b] Chemical and Biological Integrative Research Center, Korea Institute of Science and Technology, Seoul, 02792, Republic of Korea
[c] KU-KIST Graduate School of Converging Science and Technology, Korea University, Seoul, 02841, Republic of Korea
[d] Department of Chemistry, Korea University, Seoul, 02841, Republic of Korea
[e] Materials Architecturing Research Center, Korea Institute of Science and Technology, Seoul, 02792, Republic of Korea
[f] School of Biomedical Sciences and Engineering, Guangzhou International Campus, South China University of Technology, Guangzhou, 511442, China
[g] Department of Chemistry and Chemical Biology, Rutgers University, Piscataway, NJ, 08854, USA
[h] Terasaki Institute for Biomedical Innovation, Los Angeles, CA, 90064, USA
[i] State Key Laboratory of Chemo/Biosensing and Chemometrics, College of Chemistry and Chemical Engineering, Hunan University, Changsha, 410082, China
[j] Department of Biomedical-Chemical Engineering, The Catholic University of Korea, Gyeonggi-do, 14662, Republic of Korea
[k] Electronic Materials Research Center, Korea Institute of Science and Technology, Seoul, 02792, Republic of Korea
[l] KIST-SKKU Carbon-Neutral Research Center, Sungkyunkwan University (SKKU), Suwon, 16419, Republic of Korea
[m] Department of Orthopedic Surgery, Korea University Anam Hospital, Seoul, 02841, Republic of Korea
[n] Department of Electrical and Electronic Engineering and Joint Appointment with School of Biomedical Sciences, The University of Hong Kong, Hong Kong, 518057, China
[o] Department of Chemistry and Nanoscience, Ewha Womans University, Seoul, 03760, Republic of Korea
[p] Division of Engineering in Medicine, Department of Medicine, Brigham and Women's Hospital Harvard Medical School, Cambridge, MA, 02139, USA
[q] Division of Nano & Information Technology, KIST School, Korea University of Science and Technology (UST), Seoul, 02792, Republic of Korea
[r] College of Medicine, Korea University, Seoul, 02841, Republic of Korea
[s] Division of Materials Science and Engineering, Hanyang University, Seoul, 04763, Republic of Korea

## ARTICLE INFO

*Keywords:*
Dynamic self-assembly
Ligand nanospacing
*In vivo* tracking
Stem cell adhesion
Stem cell fate

## ABSTRACT

Extracellular matrix (ECM) undergoes dynamic inflation that dynamically changes ligand nanospacing but has not been explored. Here we utilize ECM-mimicking photocontrolled supramolecular ligand-tunable $Azo^{+}$ self-assembly composed of azobenzene derivatives ($Azo^{+}$) stacked via cation-π interactions and stabilized with RGD ligand-bearing poly(acrylic acid). Near-infrared-upconverted-ultraviolet light induces *cis*-$Azo^{+}$-mediated inflation that suppresses cation-π interactions, thereby inflating liganded self-assembly. This inflation increases nanospacing of "closely nanospaced" ligands from 1.8 nm to 2.6 nm and the surface area of liganded self-

Peer review under responsibility of KeAi Communications Co., Ltd.
* Corresponding author. Materials Architecturing Research Center, Korea Institute of Science and Technology, Seoul, 02792, Republic of Korea.
** Corresponding author. Chemical and Biological Integrative Research Center, Korea Institute of Science and Technology, Seoul, 02792, Republic of Korea.
*** Corresponding author. Department of Materials Science and Engineering, Korea University, Seoul, 02841, Republic of Korea.
*E-mail addresses:* msekorea@kist.re.kr (H.S. Jang), sehoonkim@kist.re.kr (S. Kim), heeminkang@korea.ac.kr (H. Kang).
[1] These authors contribute equally to this work.

https://doi.org/10.1016/j.bioactmat.2023.12.011
Received 13 May 2023; Received in revised form 30 November 2023; Accepted 14 December 2023
Available online 26 December 2023

assembly that facilitate stem cell adhesion, mechanosensing, and differentiation both *in vitro* and *in vivo*, including the release of loaded molecules by destabilizing water bridges and hydrogen bonds between the $Azo^+$ molecules and loaded molecules. Conversely, visible light induces *trans*-$Azo^+$ formation that facilitates cation-π interactions, thereby deflating self-assembly with "closely nanospaced" ligands that inhibits stem cell adhesion, mechanosensing, and differentiation. In stark contrast, when ligand nanospacing increases from 8.7 nm to 12.2 nm via the inflation of self-assembly, the surface area of "distantly nanospaced" ligands increases, thereby suppressing stem cell adhesion, mechanosensing, and differentiation. Long-term *in vivo* stability of self-assembly via real-time tracking and upconversion are verified. This tuning of ligand nanospacing can unravel dynamic ligand-cell interactions for stem cell-regulated tissue regeneration.

## 1. Introduction

Native microenvironment contains cell-adhesive proteins that are assembled into a connective network to form extracellular matrix (ECM) that dynamically interacts with cells [1]. Tissues and organs, such as cardiac tissue [2], ligament [3], lung [4], and brain [5] dynamically inflate and deflate via dynamic changes in the volume and regulate structure of the surrounding ECM. This inflation and deflation of the ECMs (including cell-adhesive Arg-Gly-Asp (RGD) ligand) can dynamically regulate integrin-RGD binding that modulates stem cell focal adhesion and mechanotransduction [6–8]. For instance, contraction of the dermal sheath drives stem cells to regenerate the tissue structure [9,10] whereas mesenchymal stem cells promote skin regeneration accelerating tissue expansion [11,12]. These reports suggest that dynamic control of the inflation and deflation of ECM-emulating ligand assemblies can help to decipher and regulate the dynamic interplay between stem cells [13–16] and the assembled ligands [17–21].

Diverse materials have been designed to realize remote manipulability [22–25] of cell-material interplay via magnetic field [26–38] or ultraviolet (UV)-free light [20,39–45] to acquire superior tissue penetrability for *in vivo* applications. Photoisomers can undergo photoisomerization in response to dual- or single-wavelength light in the range of UV and visible (Vis) light wavelengths [46], thus enabling the cell regulation [47]. Instead of utilizing tissue-absorptive UV light [48], the use of tissue-penetrable near-infrared (NIR) with upconverting nanotransducers (UCNTs) can activate light-responsive molecules via upconverted light [49–51] that regulates stem cell differentiation *in vivo* without cyclic controllability [52]. Hence, light-based *in situ*, dynamic, multimodal, and cytocompatible *in vivo* manipulation necessitates the development of materials that are differentially responsive to light stimuli.

Self-assembly of inorganic nanomaterials has been developed by nanoparticle clustering [53–57] that poses difficulties to encapsulate molecules. Supramolecular self-assembly is advantageous in loading diverse molecules within structures via intermolecular interactions [58–63]. Dynamic change in the size of supramolecular self-assembly [64] has been recently demonstrated but this requires harsh environment that cannot be utilized for biomedical applications [65–67]. Interestingly, *in situ* self-assembly [68,69] or polymerization [70] in the presence of cells has been recently reported but they have not demonstrated remote controllability *in vivo*. Developing liganded self-assembly with *in situ* dynamic change in the size via remotely controllable light stimuli can simultaneously regulate the level of bioactive ligand interaction with stem cells and molecular delivery for stem cell regulation *in vivo*.

In this study, we show that UV-free dual-wavelength laser-based control of cation-π interactions [71] enables cyclic photocontrollable inflation and deflation of RGD ligand-tunable $Azo^+$ self-assembly for stem cell regulation. We present photocontrollable system composed of azobenzene derivative cations ($Azo^+$) including hydrophobic spacer and positive charges self-assembled via cation-π and π-π interactions that are stabilized by ligand-anchored poly(acrylic acid) (PAA polyanions) via electrostatic interactions (Scheme 1). Previous works that utilized azobenzene derivative-based photocontrollable system typically included π-π interactions in weak bond strength without cation-π interactions [72,73]. Previous works have also shown the modulation of cation-π interactions but did not show remote controllability [74,75]. In addition, previous works have reported the static modulation of RGD ligand in hydrogels for stem cell [76–80]. In the present study, we demonstrate dynamic morphology control of RGD ligand-bearing hydrogels for stem cell regulation via light-mediated modulation of cation-π interactions.

We adjust the ratio of conjugated ligand density to PAA to obtain nearly continuous liganded surface ("closely nanospaced"). These self-assemblies are anchored to the UCNT-β-carotene-grafted material surface that enable dual-wavelength laser-based dynamic manipulation of self-assemblies with closely nanospaced ligands and molecular delivery, encapsulated dexamethasone (Dex) molecules via water bridges and hydrogen bonds (Scheme 2). Predominant NIR-to-UV transduction of UCNT-β-carotene triggers *trans*-to-*cis* isomerization of $Azo^+$ molecules and thus inhibit cation-π interactions between them. This resulted in the inflation of $Azo^+$ self-assemblies with closely nanospaced ligands and the release of loaded Dex molecules, which stimulate the focal adhesion-assisted mechanosensing and differentiation of stem cells both *in vitro* and *in vivo*. In contrast, Vis laser facilitated cation-π interactions via *cis*-to-*trans* isomerization that resulted in the deflation of self-assemblies with closely nanospaced ligands and stabilized molecular loading via water bridges and hydrogen bonds.

## 2. Materials and methods

### 2.1. Preparation of ligand-tunable $Azo^+$ self-assemblies

Cyclic RGD ligand (Cyclo-RGDyK, molecular weight = 620 g/mol) was conjugated to poly(acrylic acid) (molecular weight = 1.8 kDa) polyanions at a ratio of (the number of conjugated ligand):(the number of acrylic acid units in poly(acrylic acid) backbone) = $1:10^2$ via amide conjugation to endow ligand-tunable $Azo^+$ self-assemblies with the cell-adhesive property. Lysine-bearing cyclic RGD ligand (20 mg, 0.032 mmol from AnaSpec Inc.), poly(acrylic acid) (232 mg, 0.13 mmol), (benzotriazol-1-yloxy)tris(dimethylamino)phosphonium hexafluorophosphate (BOP, 114 mg, 0.26 mmol), and 1-hydroxybenzotriazole hydrate (HOBt, 34.8 mg, 0.26 mmol) were mixed in dimethylformamide (DMF, 4 mL). N,N-Diisopropylethylamine (DIPEA, 66.8 mg, 0.52 mmol) was added to the reaction solution and then stirred at room temperature for 16 h under a nitrogen atmosphere. Ligand-conjugated poly(acrylic acid) anions were obtained after dialysis using DI water and a dialysis bag (100–500 Da) to remove any unreacted reagents. RGD ligand conjugation to poly(acrylic acid) was confirmed via $^1$H NMR analysis. New $^1$H NMR peaks after amide coupling reaction between RGD ligand and poly(acrylic acid) were indexed in $^1$H NMR spectra.

To modulate the ligand nanospacing to regulate stem cell adhesion, ligand-conjugated poly(acrylic acid) at varying ratio of conjugated ligands to poly(acrylic acid) backbone was synthesized at a ratio of (the number of conjugated ligand):(the number of acrylic acid units in poly (acrylic acid) backbone) = $1:10^3$, $1:10^4$, and $1:10^5$ by only reducing the amount of Cyclo-RGDyK to 2 mg, 0.2 mg, and 0.02 mg, respectively. As control group, scrambled RGD ligand (RAD)-conjugated poly(acrylic

acid) was synthesized using Cyclo-RADfK (20 mg, 0.032 mmol from Anaspec Inc.) instead of Cyclo-RGDyK using the above procedure.

The $Azo^+$ cations were facilitated to self-assemble via cation-π and π-π interactions that incorporated ligand-conjugated poly(acrylic acid) anions via electrostatic interactions. $Azo^+$ cations (3 mg, 3.4 μmol, molecular weight: 439 g/mol) dissolved in PBS (6 mL) were added to ligand-conjugated poly(acrylic acid) anions (60 mg, 16.8 μmol) dissolved in PBS (6 mL), followed by sonication for 10 min to mediate $Azo^+$-ligand self-assembly. Afterwards, the solution was centrifuged at 800 rpm for 5 min to remove large aggregates. The uniformly sized ligand-tunable $Azo^+$ self-assemblies in the supernatant were later tethered to the upconversion nanotransducer-β-carotene-grafted material to produce ligand-bearing self-assemblies on the upconversion nanotransducer-β-carotene surface.

### 2.2. *Measurement of the number of RGD ligands and ligand nanospacing in the inflated and deflated ligand-tunable $Azo^+$ self-assemblies*

The number of RGD ligands within ligand-tunable $Azo^+$ self-assemblies was quantified via the A280 method (NanoDrop 2000 Spectrophotometer, Thermofisher Scientific) to calculate ligand nanospacing and verify that ligand-tunable $Azo^+$ self-assemblies contain sufficient saturated cell-adhesive RGD ligands. This ensures that closely nanospaced ligand surface is maintained during both their inflation and deflation that effectively regulate stem cell adhesion. Ligand-tunable $Azo^+$ self-assemblies were formed in suspension, after which ultraviolet (365 nm, 0.25 W/cm$^2$) or visible (448 nm, 0.2 W/cm$^2$) laser was subsequently applied for 1 min or 10 min, respectively. The inflated or deflated self-assemblies were centrifuged at 1000 rpm for 10 min, which was then removed via filtration through a filter (1.2 μm pore size) and the supernatant was retained. The unreacted ligand amount in the supernatant was measured and then subtracted from originally supplied ligand amount to estimate the reacted ligand amount incorporated in the inflated or deflated ligand-tunable $Azo^+$ self-assemblies. This number was divided by the number of ligand-tunable $Azo^+$ self-assemblies counted using a hemocytometer to obtain (total number of ligands per $Azo^+$ self-assemblies with ligand:AA = 1:10$^2$) in the deflated and inflated states.

To calculate ligand nanospacing of ligand-tunable $Azo^+$ self-assemblies, we assume that "virtual space occupied by each ligand" exists as spheres in a close contact one another that constitute the total space of each ligand-tunable $Azo^+$ self-assembly. Therefore, the following equation is derived:

(Virtual spherical volume occupied by each ligand: referred to as "A") = (Spherical volume of each ligand-tunable $Azo^+$ self-assembly: referred to as "B")/(total number of ligands per ligand-tunable $Azo^+$ self-assembly: referred to as "C")

"B" (spherical volume of each ligand-tunable $Azo^+$ self-assembly) is calculated by using the diameter (D) of ligand-tunable $Azo^+$ self-assembly in the deflated and inflated states $= \frac{4}{3}\pi\left(\frac{D}{2}\right)^3$

"C" (total number of ligands per ligand-tunable $Azo^+$ self-assembly) in the deflated and inflated states was obtained by the calculation using the A280 method.

Therefore, using the calculated values of "B" and "C", A (virtual spherical volume occupied by each ligand) can be obtained as the following: $A = \frac{4}{3}\pi r^3$ = "B/C" where "2r" is "the diameter of virtual sphere occupied by each ligand" that equals to "ligand nanospacing in ligand-tunable $Azo^+$ self-assembly".

Finally, (ligand nanospacing in ligand-tunable $Azo^+$ self-assembly)

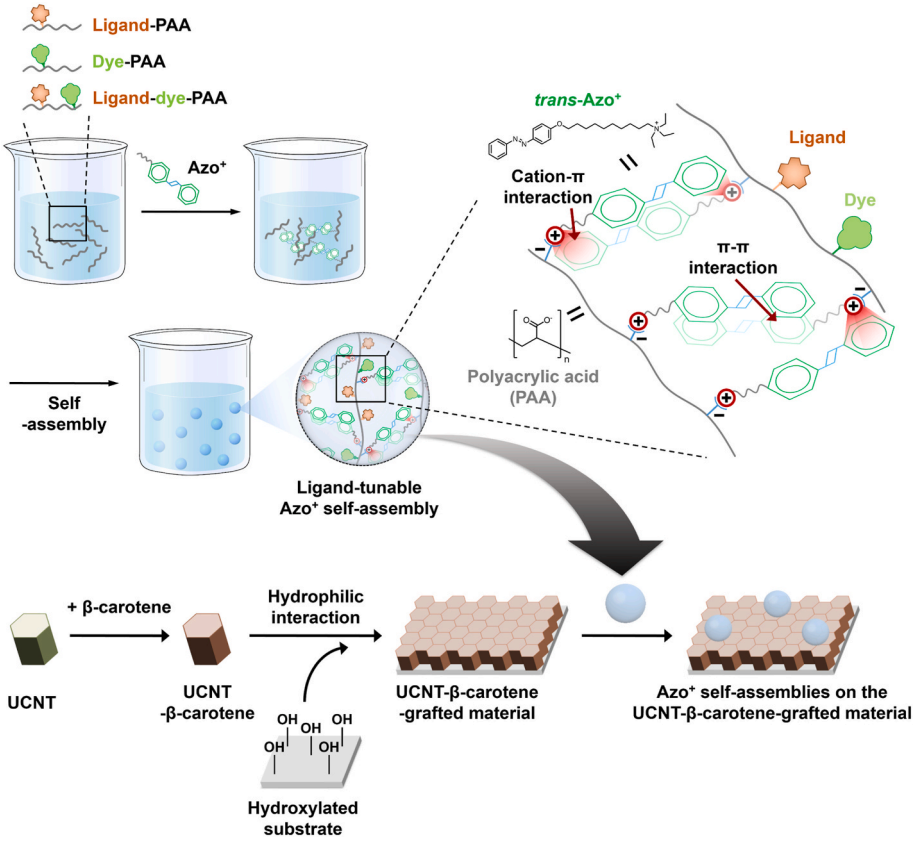


**Scheme 1.** Schematic illustration of fabrication of material preparation. The spontaneous self-assembly of azobenzene derivative cations ($Azo^+$) stacked via cation-π and π-π interactions that electrostatically attract PAA polyanions to form ligand-tunable $Azo^+$ self-assembly. The versatile conjugation of ligands and dyes to PAA polyanions empower the functionality to $Azo^+$ self-assembly. Upconversion nanotransducers (UCNTs) are coated with β-carotene and are grafted to the hydroxylated substrate through hydrophilic interaction. Then, $Azo^+$ self-assemblies are anchored to UCNT-β-carotene-grafted material.

= 2r = 2 x (radius of virtual space occupied by RGD) = 2 $x\sqrt[3]{\frac{3\times(A:\text{Virtual spherical volume occupied by each ligand})}{4\pi}}$.

Using the above calculations, the ligand nanospacing of ligand-tunable $Azo^+$ self-assembly including ligand-conjugated poly(acrylic acid) was estimated to be 1.8 nm and 2.6 nm in deflated and inflated states, respectively, which used the ligand-conjugated poly(acrylic acid) with ligand:AA = $1:10^2$.

To further modulate the ligand nanospacing of ligand-tunable $Azo^+$ self-assembly, ligand-conjugated poly(acrylic acid) was synthesized with ligand:AA = $1:10^3$, $1:10^4$, or $1:10^5$, respectively. When using the ligand-conjugated poly(acrylic acid) with ligand:AA = $1:10^3$, the ligand nanospacing was calculated to be 4.0 nm and 5.7 nm in the deflated and inflated states, respectively. When using the ligand-conjugated poly (acrylic acid) with ligand:AA = $1:10^4$, the ligand nanospacing was calculated to be 8.7 nm and 12.2 nm in the deflated and inflated states, respectively. When using the ligand-conjugated poly(acrylic acid) with ligand:AA = $1:10^5$, the ligand nanospacing was calculated to be 18.6 nm and 26.4 nm in the deflated and inflated states, respectively.

### 2.3. *In vivo* regulation of stem cells via NIR and Vis laser-based time-regulated conversion of ligand-tunable $Azo^+$ self-assemblies

As a model for the *in vivo* translation of regulation of stem cell focal adhesion, mechanotransduction, and differentiation via tissue-penetrative ultraviolet-free dual-wavelength (near-infrared and visible) laser, Dex-loaded ligand-tunable $Azo^+$ self-assemblies including the ligand-conjugated poly(acrylic acid) with ligand:AA = $1:10^2$ (closely nanospaced ligands) on the upconversion nanotransducer (core/shell)-β-carotene-grafted material (silicon substrate) were subcutaneously implanted into balb/c nude mice. Robust silicon subsrate was used in place of glass substrate since they present an identical surface chemistry due to the native oxide formation on the silicon substrate surface. Forty-eight three-month-old balb/c mice were used in the experiment after receiving approval from the Institutional Animal Care and Use Committee at Korea University. The mice were first subjected to anesthesia using a mixture of alfaxan (75 μL) and rompun (25 μL) via intraperitoneal injection, after which 1.8 cm-long incisions were made on their backs. After implantation of Dex-loaded ligand-tunable $Azo^+$ self-assemblies on the upconversion nanotransducer (core/shell)-β-carotene-grafted material, the incisions were carefully sutured and approximately 30,000 hMSCs were injected onto each piece of implanted material. Following implantation, *in situ* cyclic inflation and deflation of ligand-tunable $Azo^+$ self-assemblies was remotely manipulated via replicating or changing applying near-infrared laser (980 nm, 1 W/$cm^2$) for 1 min or visible laser (488 nm, 0.2 W/$cm^2$) for 10 min onto the backs of the mice every 3 h for the time-regulated photoconversion of ligand-tunable $Azo^+$ self-assemblies. Their effect on the stem cell focal adhesion, mechanosensing, and differentiation was investigated after 6 h via confocal immunofluorescence microscopy.

To explore osteogenic differentiation of stem cells *in vivo* using a late osteoblast marker (osteocalcin), *in situ* time-regulated inflation and deflation of ligand-tunable $Azo^+$ self-assemblies including the ligand-conjugated poly(acrylic acid) with ligand:AA = $1:10^2$ was remotely manipulated via replicating or changing applying near-infrared laser (980 nm, 1 W/$cm^2$) for 1 min or visible laser (488 nm, 0.2 W/$cm^2$) for 10 min onto the backs of the mice every 12 h for the time-regulated photoconversion of the $Azo^+$-ligand self-assemblies after implantation. At 72 h after implantation, the samples were collected and subjected to

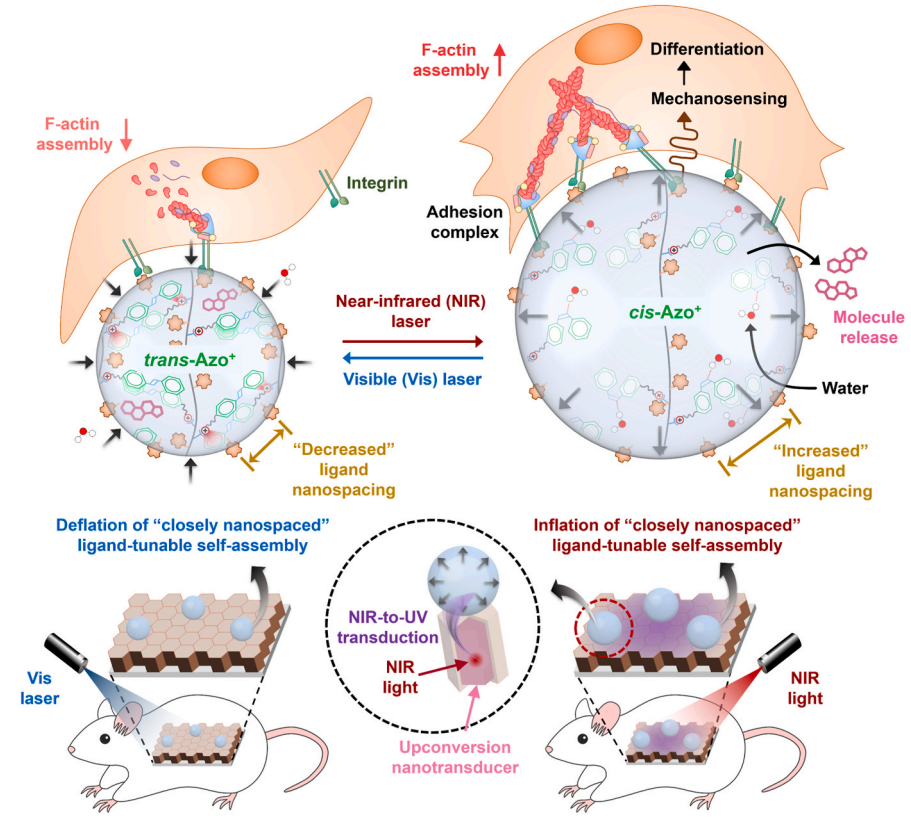


**Scheme 2.** Schematic demonstration of conceptual summary of this study. NIR-to-UV transduction by upconversion nanotransducers (UCNTs) and Vis-absorptive β-carotene grafted to material surface inhibits cation-π interactions that induces inflated state of *cis*-$Azo^+$ self-assembly with "closely nanospaced" ligands when using ligand:AA = $1:10^2$. This also facilitates the release of loaded molecules that stimulate stem cell mechanosensing and differentiation *in vivo*. Conversely, Vis laser mediates cation-π interactions that induce deflated state of *trans*-$Azo^+$-ligand self-assembly with "closely nanospaced" ligands that deactivates stem cell mechanosensing and differentiation *in vivo*.

immunocytochemical staining.

### 2.4. Real-time long-term in vivo stability of ligand-tunable $Azo^+$ self-assemblies that are placed on the UCNT-grafted material in live animal

To evaluate long-term *in vivo* stability of $Azo^+$ -ligand self-assemblies including the ligand-conjugated poly(acrylic acid) with ligand:AA = $1:10^2$ anchored on the upconversion nanotransducer-grafted material, fluorescence intensity of $Azo^+$-dye self-assemblies was measured. Male nude mice (6–8 weeks) were anesthetized by an intraperitoneal injection of 100 μL of rompun and alfaxan mixture of 1:2 (v/v) ratio. $Azo^+$-dye self-assemblies on upconversion nanotransducer-grafted substrate (11 mm × 11 mm) was implanted subcutaneously on the lateral side of nude mice. Here, β-carotene was not used since its fluorescence spectra overlaps with an absorption spectra of fluorescein dye. At 0 d, 7 d, 14 d, 21 d, 28 d and 35 d post-implantation, we collected the implanted sample from mice and measured the fluorescence intensity of $Azo^+$-dye self-assembly at 511 nm using Hitachi F-7000 spectrophotometer under application of 980 nm NIR laser. Fluorescence intensity of $Azo^+$-dye self-assembly at 511 nm was selected to obtain Förster resonance energy transfer (FRET)-like signal arising from NIR-to-Vis light transduction of UCNT and sequential Vis light absorption and green fluorescence light emission of fluorescein cadaverine dye.

In addition, 980 nm laser was installed in IVIS spectrum *in vivo* imaging system (Caliper, USA) for *in vivo* monitoring fluorescence signal from $Azo^+$ -dye self-assembly. At 0 d, 3 d, 7 d, 14 d, and 21 d post-implantation, fluorescein signals from mice were repeatedly imaged with 980 nm laser (1 W/$cm^2$) irradiation. This provides a methodology to demonstrate the system stability by generating fluorescence signals sensitive to interaction between ligand-tunable $Azo^+$ self-assemblies and upconversion nanotransducer-grafted materials within the 10 nm range.

To confirm the *in vivo* stability of ligand-tunable $Azo^+$ self-assemblies including the ligand-conjugated poly(acrylic acid) with ligand:AA = $1:10^2$, fluorescent-dye-incorporated $Azo^+$-ligand self-assemblies on the upconversion nanotransducer-β-carotene-grafted material were implanted for 6 h. The number of stably remaining ligand-tunable $Azo^+$ self-assemblies was fluorescently tracked using a confocal microscope before and after *in vivo* implantation.

### 2.5. Long-term in vivo stability of the UCNT-β-carotene-grafted material

Long-term *in vivo* stability of upconversion nanotransducer-β-carotene-grafted materials was also assessed. Upconversion nanotransducer-β-carotene-grafted substrate (7 mm × 7 mm) was implanted subcutaneously on the lateral side of nude mice. At 0 d, 7 d, 14 d, 21 d, 28 d and 35 d post-implantation, the upconversion nanotransducer-β-carotene-grafted substrates were collected and subjected to photoluminescence measurement. We measured the photoluminescence intensity of UCNT-β-carotene-grafted material at 807 nm (distinct photoluminescence peak wavelength) using Hitachi F-7000 spectrophotometer under application of 980 nm NIR laser.

At 0 d, 1 d, 3 d, and 7 d post-implantation, the upconversion nanotransducer-β-carotene-grafted substrates were collected and subjected to photoluminescence measurement to evaluate the maintenance of transduced UV/Vis ratio.

## 3. Results and discussion

### 3.1. Tuning of the UCNTs with core/shell nanostructure and β-carotene enables predominant NIR-to-UV transduction with high photoluminescence intensity

UV-free dual-wavelength (NIR and Vis) laser-based bimodal manipulation of ligand-tunable $Azo^+$ self-assemblies necessitates predominant NIR-to-UV transduction in high photoluminescence intensity over NIR-to-Vis transduction. The upconverted UV specifically triggers *trans*-to-*cis* $Azo^+$ photoisomerization, while Vis laser directly triggers *cis*-to-*trans* $Azo^+$ photoisomerization. To enhance the photoluminescence intensity and transduced UV/Vis ratio, we designed $NaYF_4$:Yb,Tm UCNT core to incorporate dual lanthanide dopants of ytterbium (Yb) and thulium (Tm) elements, which was coated with an epitaxially grown $NaYF_4$ shell to yield UCNT ($NaYF_4$:Yb,Tm core/$NaYF_4$ shell) to passivate surface defects arising from dangling bonds [81]. The Yb- and Tm-doped UCNTs exhibited effective upconversion in deeply lying tissues in response to NIR laser illumination, thus making them suitable for *in vivo* applications. To further elevate the NIR-transduced UV/Vis ratio, we coated the surface of the UCNTs ($NaYF_4$:Yb,Tm core/$NaYF_4$ shell) with naturally occurring β-carotene used in clinics [82], which absorbs light in the Vis region (400–500 nm), to selectively absorb the NIR-transduced-Vis light but not the NIR-transduced-UV light (Fig. S1). The uniform distributions of sizes and dual lanthanide dopants of the UCNT core and the UCNT (core/shell) were confirmed by using high-angle annular dark-field scanning transmission electron microscopy (HAADF-TEM), elemental mapping images, and dynamic light scattering (DLS) analysis (Figs. S2 and S3). The computed hydrodynamic size of the UCNTs (core/shell) was 49.0 ± 3.0 nm. The epitaxial $NaYF_4$ shell growth on the surface of $NaYF_4$:Yb,Tm UCNT core was shown to be free of defects via high-resolution TEM (HR-TEM) imaging (Fig. S2A). Crystal structures of UCNT core only and UCNTs were analyzed by X-ray diffraction (XRD), confirming the formation of hexagonal $NaYF_4$ crystals (Fig. S2C).

Photoluminescence spectra of the $NaYF_4$:Yb,Tm UCNT core revealed NIR laser-excited emission in both the UV and Vis regions due to the presence of the Tm dopant, which was substantially elevated in the UCNT ($NaYF_4$:Yb,Tm core/$NaYF_4$ shell) (Fig. S4A). The UCNT (core/shell) coated with β-carotene significantly absorbed light in the blue region (400–500 nm), thereby suggesting efficient absorption of NIR-to-Vis transduction (Fig. S4B). Successful β-carotene coating on the UCNT (core/shell) was cross-confirmed by DLS analysis, UV–Vis absorbance, and thermogravimetric analysis (TGA) (Figs. S3, S5, and S6). DLS analysis showed considerable increase in hydrodynamic size upon the coating of β-carotene onto the UCNTs (Fig. S3). UV–Vis absorbance showed that UCNT-β-carotene exhibited high absorption in the Vis light region (400 nm–500 nm) similar to that of β-carotene, suggesting that NIR-to-Vis-transduced light is selectively absorbed (Fig. S5). Thermogravimetric analysis (TGA) of UCNT-β-carotene showed weight loss due to the presence of β-carotene (organic molecules), which was not found in that of the UCNTs without β-carotene, thereby confirming successful β-carotene coating on UCNTs (Fig. S6).

The UCNT (core/shell)-β-carotene structure was homogeneously and fully grafted to the material surface as demonstrated by field-emission scanning electron microscopy (FE-SEM) imaging (Fig. S7A). Consistently, the NIR-transduced UV/Vis intensity ratio in the UCNT (core/shell)-β-carotene-grafted material was significantly elevated compared with that without β-carotene (Figs. S7B and C). These findings prove that the UCNT (core/shell)-β-carotene-grafted material exhibits predominant NIR-to-UV transduction with high photoluminescence intensity while efficiently suppressing NIR-to-Vis transduction.

### 3.2. Dual-wavelength-light-controlled cation-π interactions for cyclic changing of inflation and deflation of ligand-tunable $Azo^+$ self-assembly

To explore the feasibility of dual-wavelength-laser-controllable liganded self-assemblies involving dynamic changes in their size, cationic $Azo^+$ molecules with aromatic rings, hydrophobic spacers, and $N^+$ were synthesized via serial modification of azobenzene from Azo-OH to Azo-Br and then to $Azo^+$ molecules (Fig. S8). These molecules were designed to facilitate cation-π, which serves as physical crosslinking point [83] between the $Azo^+$ molecules to produce liganded ($Azo^+$-ligand) self-assemblies. $^1$H nuclear magnetic resonance (NMR) analysis revealed the peaks corresponding to phenolic group in the Azo-OH molecule, an ether group in the Azo-Br molecule, and α-hydrogens to tertiary amine group in the $Azo^+$ molecule (Fig. S9). $^{13}$C NMR

analysis confirmed new peaks for specific carbons corresponding to hydrophobic spacer in the Azo-Br molecule and tertiary amine group in the Azo$^+$ molecule (Fig. S10). High-resolution mass spectrometry (HRMS) showed increase in molecular weights when converting Azo-OH molecule to Azo-Br molecule and then to Azo$^+$ molecule, which were comparable to theoretically calculated molecular weights (Fig. S11).

RGD ligand-conjugated PAA polyanions synthesized via an amide coupling reaction facilitated electrostatic interactions between the anionic PAA and the cationic Azo$^+$ molecule to become incorporated into the ligand-tunable Azo$^+$ self-assemblies (Fig. S12). Successful synthesis of RGD ligand-conjugated PAA via amide bond formation between RGD ligand and PAA was confirmed by $^1$H NMR spectra and Fourier transform infrared (FTIR) spectroscopy (Figs. S13 and S14). By mixing synthesized Azo$^+$ molecules with ligand-conjugated PAAs at the critical self-assembly concentration (0.91 mg/mL), ligand-tunable Azo$^+$ self-assemblies were formed (Fig. 1A). The concentration of 5.12 mg/mL was determined to obtain the self-assembly at considerable size and therefore used for all the experiments in this study. PAA with different

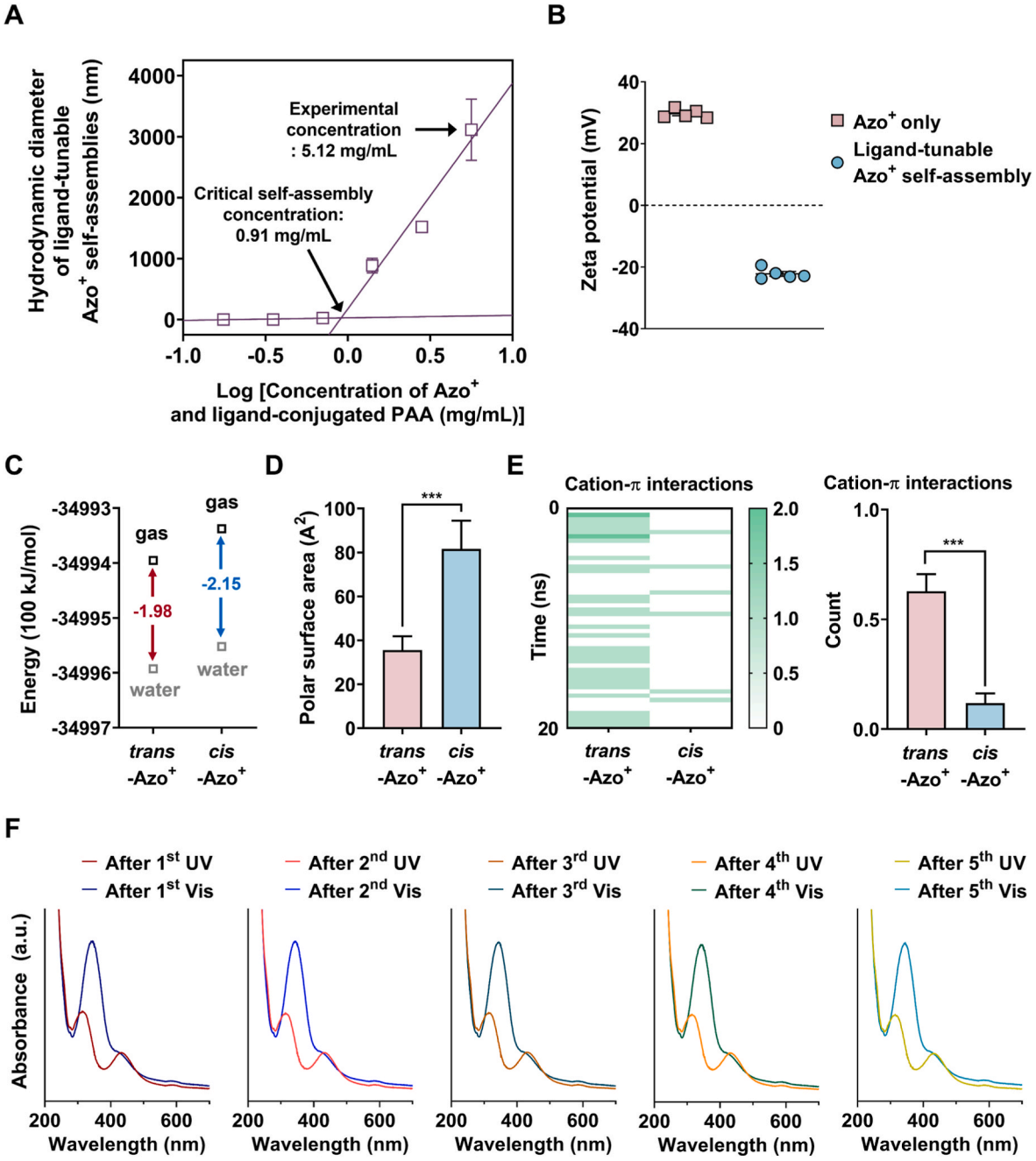


**Fig. 1.** Rapid cyclic photocontrollable conversion of ligand-tunable Azo$^+$ self-assembly is modulated by cation-π interactions. (A) Critical precursor concentration for ligand-tunable Azo$^+$ self-assembly formation. Data are shown as the mean ± standard error (n = 6). (B) Changes in surface charges of after formation of ligand-tunable Azo$^+$ self-assemblies. Data are shown as the mean ± standard error (n = 5). (C) Density functional theory (DFT) simulations of the hydration energies of the *trans*-Azo$^+$ and *cis*-Azo$^+$ molecules. (D) Molecular dynamics (MD) simulations (0–20 ns) of the average polar surface area (A$^2$) of *trans*-Azo$^+$ and *cis*-Azo$^+$ molecules. (E) MD simulations of a heat map chart with corresponding frequency counts of cation-π interactions. MD simulation images shown in Fig. S18 were used for the quantifications. (F) UV–Vis absorbance of ligand-tunable Azo$^+$ self-assemblies after being subjected to 5 cycles of Vis (0.2 W/cm$^2$, 30 s) and UV (0.25 W/cm$^2$, 30 s) laser application. Vis and UV laser were used to induce *trans*-Azo$^+$ and *cis*-Azo$^+$ self-assemblies, respectively. The mean ± standard error represents the data [(D) n = 500, (E) n = 50].

molecular weight (5100 Da) formed smaller $Azo^+$ self-assembly (116 ± 23 nm) compared with the diameter of $Azo^+$ self-assembly with 1800 Da PAA (3308 ± 91 nm) (Fig. S15). Since particles smaller than 1 μm can be readily endocytosed, we used PAA with molecular weight of 1800 Da to prevent the endocytosis for all the experiments throughout the study. Incorporation of $Azo^+$ and ligand-conjugated PAA into the self-assembly was confirmed by FTIR spectroscopy, which showed specific absorption peaks of both $Azo^+$ and ligand-conjugated PAA (Fig. S16). Zeta potential measurement also confirmed that $Azo^+$ cation only showed positive surface charge but ligand-tunable $Azo^+$ self-assembly showed negative surface charge due to the co-presence of $Azo^+$ cations and ligand-conjugated PAA polyanions (Fig. 1B). We have summarized control groups used for material characterization in Table S1.

The cationic $Azo^+$ molecules were self-assembled via cation-π and π-π interactions that incorporate the ligand-conjugated polyanions. Both *cis*-$Azo^+$ and *trans*-$Azo^+$ molecules were analyzed by density functional theory (DFT) simulations, which demonstrated markedly higher hydration energy (i.e., hydrophilicity) in the *cis*-$Azo^+$ than the *trans*-$Azo^+$ form (Fig. 1C). The intermolecular interactions inducing inflation of the *cis*-$Azo^+$-ligand self-assemblies and deflation of the *trans*-$Azo^+$-ligand self-assemblies were systematically analyzed via molecular dynamics (MD) simulations [84]. *cis*-$Azo^+$ molecules exhibited a significantly higher polar surface area (i.e., polarity) than *trans*-$Azo^+$ molecules (Fig. 1D). The *trans*-$Azo^+$ complex exhibited significantly higher cation-π interactions than the *cis*-$Azo^+$ complex as evidenced by representative images, heat maps, and associated frequency counts of MD simulations during 20 ns (Fig. S17). When acrylic acid (to which RGD ligand is conjugated) was incorporated into the $Azo^+$ complex, the *trans*-$Azo^+$-ligand complex consistently exhibited considerably higher cation-π interactions than the *cis*-$Azo^+$-ligand complex (Fig. 1E and S18). These findings collectively suggest that *trans*-$Azo^+$ molecules exhibit stronger cation-π intermolecular interactions and form a compactly packed structure, thereby deflating the *trans*-$Azo^+$-ligand self-assembly. In contrast, hydrophilic polar *cis*-$Azo^+$ molecules exhibit weaker cation-π intermolecular interactions and form a loosely packed structure of *cis*-$Azo^+$ molecules, thereby inflating the *cis*-$Azo^+$-ligand self-assembly that can absorb water.

Next, we explored the rapid cyclic controllability and time-dependent stability of ligand-tunable $Azo^+$ self-assemblies by manipulation of dual-wavelength laser application. The *cis*-$Azo^+$-ligand self-assemblies were inflated with substantially increasing size by UV laser application while the *trans*-$Azo^+$-ligand self-assemblies were deflated with substantially decreasing size by Vis laser application (Fig. S19). The rapid cyclic controllability between the *cis*-$Azo^+$-ligand self-assemblies (repeatedly exhibiting maximum absorbance peak at 315 nm with maximum *trans*-to-*cis* isomerized state) and the *trans*-$Azo^+$-ligand self-assemblies (repeatedly exhibiting maximum absorbance peak at 345 nm with maximum *cis*-to-*trans* isomerized state) was demonstrated after alternating application of UV and Vis laser for 30 s each for 5 cycles, as evidenced via UV–Vis spectrometry (Fig. 1F and S20). Due to the instability of *trans*-to-*cis* isomerized state, its time-dependent stability was examined [46]. The majority of the *cis*-$Azo^+$-ligand self-assemblies formed after UV laser application were stably preserved for 24 h (Fig. S21). These findings justify the dual-wavelength-laser-controlled cyclic changes of ligand-tunable $Azo^+$ self-assemblies to mediate cyclic adhesion of stem cells in the day scale, which is discussed later in the manuscript.

The ligand-tunable $Azo^+$ self-assemblies were tethered to the UCNT-β-carotene-grafted material surface, which ensured that the NIR-transduced-UV light could readily reach the ligand-tunable $Azo^+$ self-assemblies. To fluorescently track ligand-tunable $Azo^+$ self-assemblies, dye-conjugated PAA was synthesized using a fluorescent dye, which was incorporated into the self-assemblies along with $Azo^+$ molecules (Fig. S22). UV–Vis spectroscopy was used to estimate the loading efficiency of dye into the self-assembly, which was 33.8 %. Then, homogeneously distributed ligand-tunable $Azo^+$-dye self-assemblies in spherical ellipsoid shape were formed on the UCNT-grafted material at a density of 4882 ± 250 self-assemblies per $mm^2$, as verified by confocal fluorescent imaging in three-dimensional (3-D) and two-dimensional (2-D) views (Fig. 2A). *In situ* real-time confocal microscopy imaging [85] showed that dual-wavelength-laser-controlled cyclic deflation, inflation, and deflation of self-assembly occurred when they remained tethered to the material surface via hydrophilic interactions (Fig. 2B and Supplementary Video S1). Accordingly, the time-resolved decrease, increase, and then decrease in the projection area, diameter, and total projection area per unit area of self-assemblies occurred (Fig. 2C, D, and E). The calculated total projection area of self-assemblies was $5.3 \pm 0.6 \times 10^4$ $\mu m^2/mm^2$ or $3.4 \pm 0.2 \times 10^4$ $\mu m^2/mm^2$ when inflated or deflated, respectively.

Under dual-wavelength laser application, the swelling ratio (wet weight/dry weight) of self-assemblies in the inflated state was found to significantly increase compared to that in the deflated state, thus proving that the inflation of *cis*-$Azo^+$-ligand self-assemblies can be attributed to facilitated water absorption by the hydrophilic and polar *cis*-$Azo^+$ molecules (Fig. 2E). A280 method using NanoDrop was used to measure and calculate total number of ligands per self-assembly at the bulk, which was estimated to be $21.1 \times 10^9 \pm 1.7 \times 10^9$ and $19.0 \times 10^9 \pm 1.0 \times 10^9$ in the inflated and deflated states without statistically significant difference (Fig. 2E). This suggests that ligand-tunable $Azo^+$ self-assemblies contain a sufficient but unchanged number of saturated ligands per self-assembly at the bulk that can efficiently regulate stem cell adhesion by independently increasing or decreasing the ligand nanospacing of closely nanospaced ligands in the self-assemblies via the inflation and deflation, respectively.

### 3.3. Dual-wavelength-laser-regulated molecular delivery by modulating water bridges and hydrogen bonds in ligand-tunable $Azo^+$ self-assemblies

We investigated the versatility of ligand-tunable $Azo^+$ self-assemblies for use as a light-responsive drug delivery vehicle. As a drug molecule model, Dex was chosen due to its osteogenesis-inductive property. Dex molecules were loaded into ligand-tunable $Azo^+$ self-assemblies to yield Dex-loaded ligand-tunable $Azo^+$ self-assemblies that contain ligand-conjugated polyanions (Fig. 3A). UV–Vis spectroscopy was used to calculate the loading efficiency of Dex into the self-assembly, which was 98.7 %. The examination of intermolecular interactions via MD simulations showed that Dex molecules were held within the $Azo^+$-ligand complex when the $Azo^+$ cations were assembled via cation-π and π-π interactions. We found that the *trans*-$Azo^+$ molecules strongly attracted Dex molecules via water bridges and hydrogen bonds within the *trans*-$Azo^+$-ligand complex, as shown by the MD simulation (Fig. 3B). Interestingly, when the *trans*-$Azo^+$ molecules underwent *trans*-to-*cis* photoisomerization, the water bridges and hydrogen bonds became destabilized so that the *cis*-$Azo^+$-molecules no longer attracted Dex molecules within the *cis*-$Azo^+$-ligand complex (Fig. 3B, C, D, and E). This suggests that Dex molecules are released by freely diffusing out of the *cis*-$Azo^+$-ligand self-assemblies inflated via facilitated water absorption. To confirm this hypothesis, we temporally regulated either replicated ("Vis/Vis" and "NIR/NIR" groups) or changed ("Vis/NIR" and "NIR/Vis" groups) UV laser application (0.25 $W/cm^2$) and Vis laser application (0.2 $W/cm^2$) for 1 min each with 30 min intervals and examined the cumulative amount of released Dex via UV–Vis spectrometry. Control group without UV and Vis laser application is also included. The results showed that Dex release was considerably stimulated after UV laser application that inflated the Dex-loaded *cis*-$Azo^+$-ligand self-assemblies, thereby weakly holding Dex molecules within the self-assemblies (Fig. 3F). Individual groups are also shown to better differentiate the release trend of various groups (Fig. S23A). In contrast, Dex release was hindered after Vis laser application that changed Dex-loaded *trans*-$Azo^+$-ligand self-assemblies from inflated state to deflated state, thereby strongly holding the Dex molecules within the self-assemblies. In addition, photocontrollable drug release

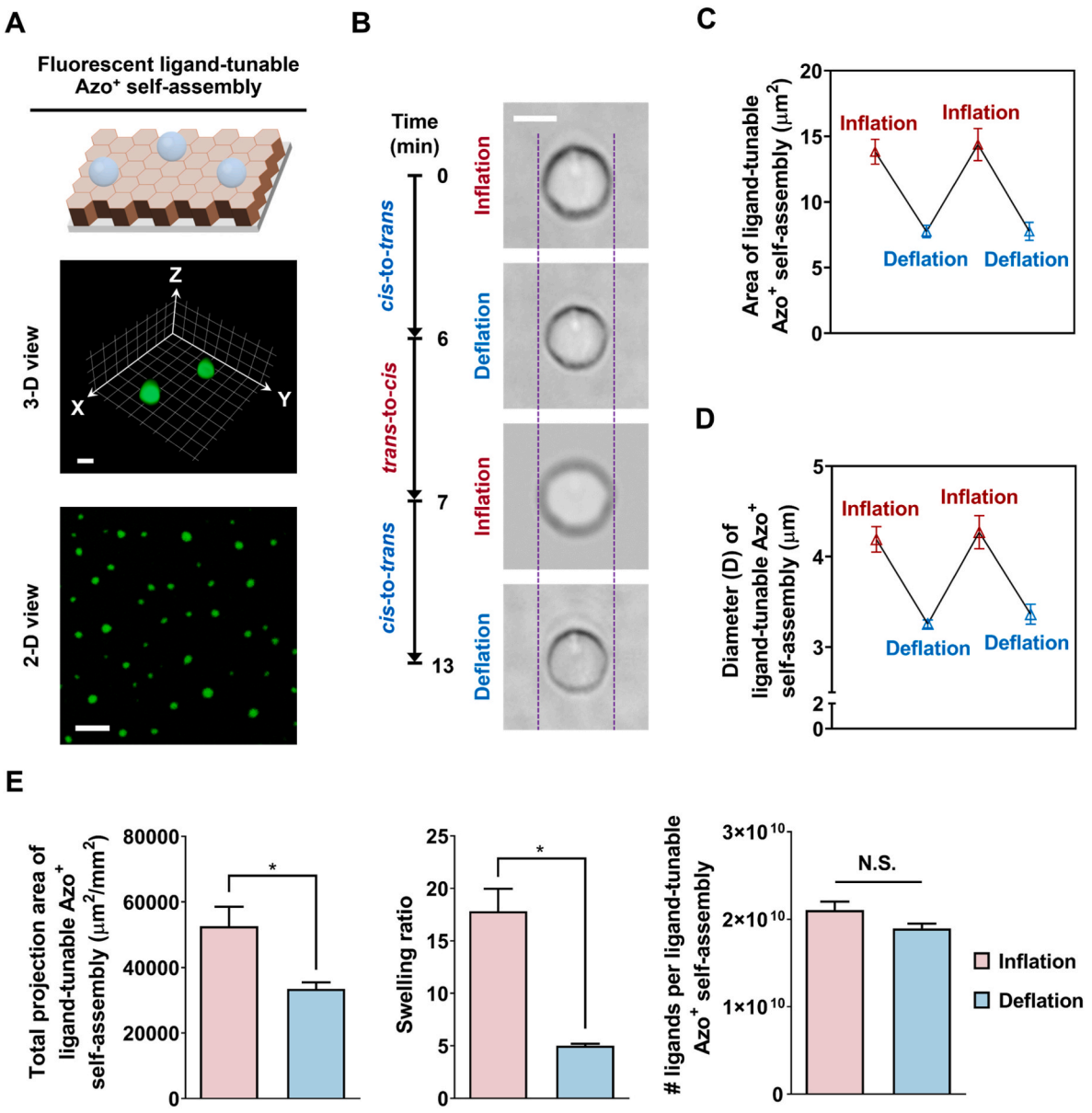


**Fig. 2.** Photocontrollable changing of the inflation and deflation of ligand-tunable $Azo^+$ self-assembly is mediated by dual-wavelength laser application. (A) Schematic and confocal fluorescence images of ligand-tunable $Azo^+$-dye self-assembly in 3-D and 2-D views. Scale bars: 2 μm (3-D view) and 10 μm (2-D view). (B) *In situ* imaging of time-lapse snapshots of the ligand-tunable $Azo^+$ self-assembly exhibiting cyclic deflation, inflation, and then deflation in response to sequential application of Vis laser (0.2 W/$cm^2$) for 6 min, UV laser (0.25 W/$cm^2$) for 1 min, and then Vis laser for 6 min. Scale bar: 3 μm. Corresponding quantification of (C) the projection area and (D) diameter of each ligand-tunable $Azo^+$ self-assembly during two cycles of inflation and deflation by using the images shown in (B). (E) The total projection area of ligand-tunable $Azo^+$ self-assemblies per unit area ($\mu m^2/mm^2$), the swelling ratio (wet weight/dry weight) of ligand-tunable $Azo^+$ self-assemblies, and total number of ligands per $Azo^+$ self-assembly with ligand:AA = $1:10^2$ in the inflated and deflated states under dual-wavelength laser application. The mean ± standard error represents the data (n = 5). Statistically significant differences are represented as asterisks (*: $p < 0.05$). Statistically non-significant differences are represented as the N.S.

ability of $Azo^+$ self-assembly was verified in two cycles of inflation and deflation of $Azo^+$ self-assembly (Fig. S23B).

### 3.4. Cyclic photocontrollable stem cell adhesion regulated by NIR and vis laser-mediated in situ changes in ligand-tunable $Azo^+$ self-assemblies

Next, we explored whether NIR and Vis laser-manipulated dynamic inflation and deflation of ligand-tunable $Azo^+$ self-assemblies can facilitate the cyclic focal adhesion of human mesenchymal stem cells (hMSCs). Prior to *in vitro* experiments, we first confirmed the biocompatibility of $Azo^+$ self-assembly and UCNT-β-carotene-grafted material (Fig. S24). Briefly explain the experimental protocol, at 0 h, stem cells were plated onto the ligand-tunable $Azo^+$ self-assemblies on the UCNT-β-carotene-grafted material. Stem cells were not plated additionally during cell culture on the substrates. Then, we only used UV-free NIR (980 nm, 1 W/$cm^2$) and Vis (488 nm, 0.2 W/$cm^2$) laser for all *in vitro* and *in vivo* experiments along with the UCNT-β-carotene-grafted material. We illuminated UV-free NIR and Vis laser onto the UCNT-β-carotene-grafted material from the top such as the NIR reached the UCNT-β-carotene and then emitted NIR-to-UV transduced light toward the ligand-tunable $Azo^+$ self-assemblies while Vis laser directly reached the ligand-tunable $Azo^+$ self-assemblies (Fig. S25A). Dual-wavelength laser was applied every 12 h and changed every 24 h for photocontrolled cyclic conversion of $Azo^+$ self-assemblies. The UCNT-β-carotene-grafted

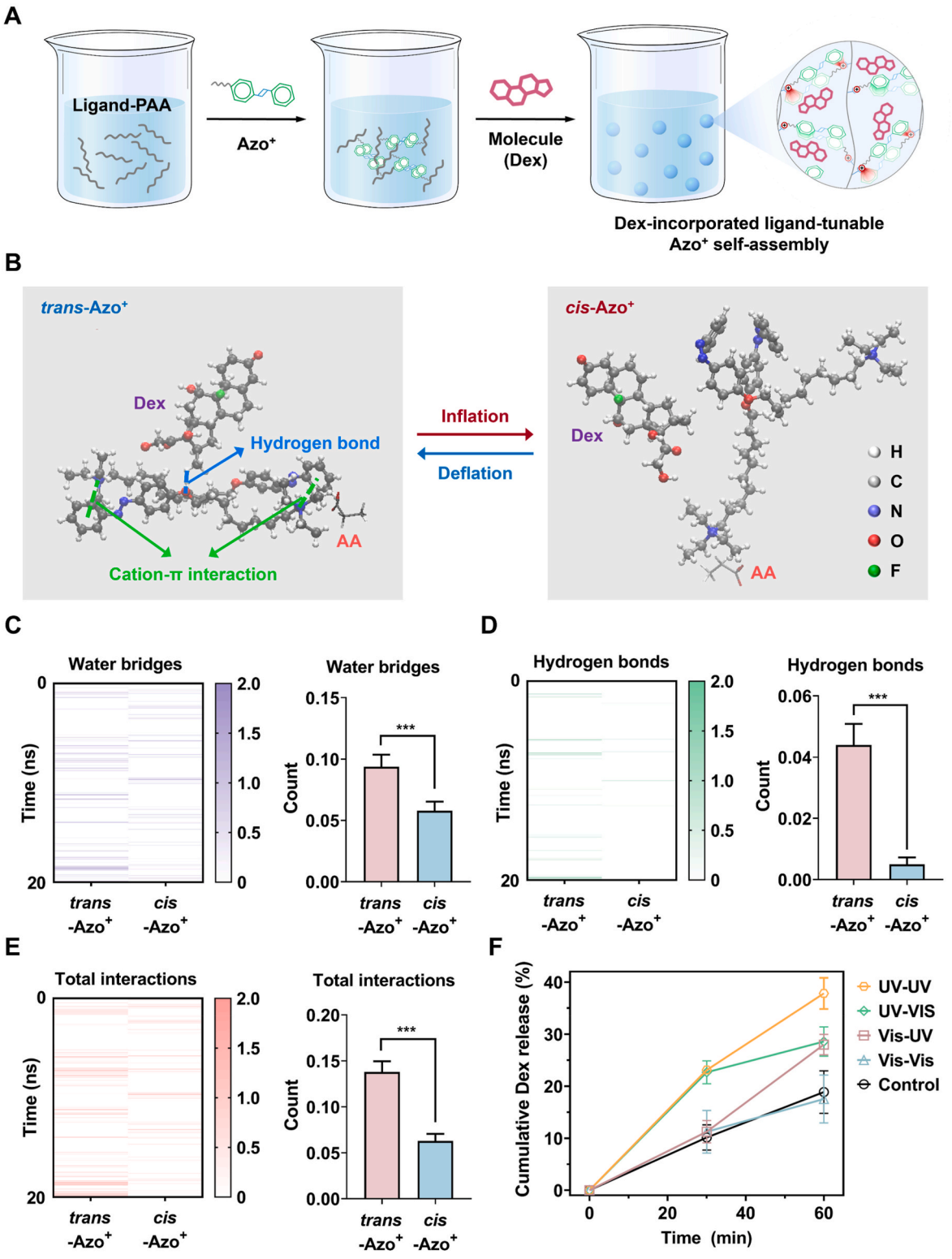


**Fig. 3.** Remotely manipulated triggering of molecular release by destabilizing water bridges and hydrogen bonds. (A) Schematic representation of loading molecule (Dex) during the self-assembly including tunable ligands and $Azo^{+}$. (B) Molecular dynamics (MD) simulations of representative images of two *trans*-$Azo^{+}$ (left) and *cis*-$Azo^{+}$ molecules (right) interacting with acrylic acid and Dex molecule. MD simulations (0–20 ns) of heat map charts of (C) water bridges, (D) hydrogen bonds, and (E) total interactions (the sum of the water bridges and hydrogen bonds) that occur between $Azo^{+}$ molecule and Dex molecule. Corresponding frequency counts for each interaction are also included. (F) The cumulative Dex release profile from Dex-loaded ligand-tunable $Azo^{+}$ self-assemblies after either replicated ("Vis/Vis" and "NIR/NIR" groups) or changed ("Vis/NIR" and "NIR/Vis" groups) UV laser application (0.25 W/cm$^2$) and Vis laser application (0.2 W/cm$^2$) for 1 min each with 30 min intervals. Control group without UV and Vis laser application is also included. UV and Vis laser were used to induce *cis*-$Azo^{+}$ and *trans*-$Azo^{+}$ self-assemblies, respectively. The mean ± standard error represents the data [(C–E) n = 1000 and (F) n = 3]. Statistically significant differences are represented as asterisks (***: $p < 0.001$).

material that facilitates predominant NIR-to-Vis transduction in the absence of ligand-tunable Azo$^+$ self-assemblies functioned as a passivation surface that suppressed the non-specific binding of biomolecules, thereby enabling ligand-specific stem cell regulation [86]. Immunofluorescence staining images demonstrate that stem cells exhibited a significantly higher number of paxillin clusters (focal adhesion complex) and F-actin filaments associated with considerably higher integrin β1 expression by "NIR"-triggered inflation of liganded self-assemblies than under the conditions of "No irradiation" or "Vis"-triggered deflation of liganded self-assemblies (Fig. S25B). Concomitantly, "NIR" laser application significantly elevated focal adhesion and adhered cell density and area with decreased aspect ratio compared with the "No irradiation" and "Vis" laser application groups (Fig. S25C).

We investigated a dominant factor that regulates stem cell adhesion. It was previously reported that different concentrations of 6.8 mM vs. 0.68 mM of RGD ligands tethered to bulk hydrogels were considered as relatively 100 % vs. 10 % RGD ligands that differentially regulate stem cell adhesion, respectively [78]. Also, it was recently shown that RGD "ligand nanospacing" below and above integrin size (10 nm) differentially regulated the level of integrin binding, cell adhesion [33], and mechanosensing. The "ligand nanospacing" below 3.5 nm below integrin size was recognized by cells as if the ligands were continuous (referred to as "closely nanospaced"), which exhibited similar cellular adhesion to completely continuous ligands with "ligand nanospacing" of 0 nm, and cell adhesion is regulated by "closely nanospaced" liganded surface area.

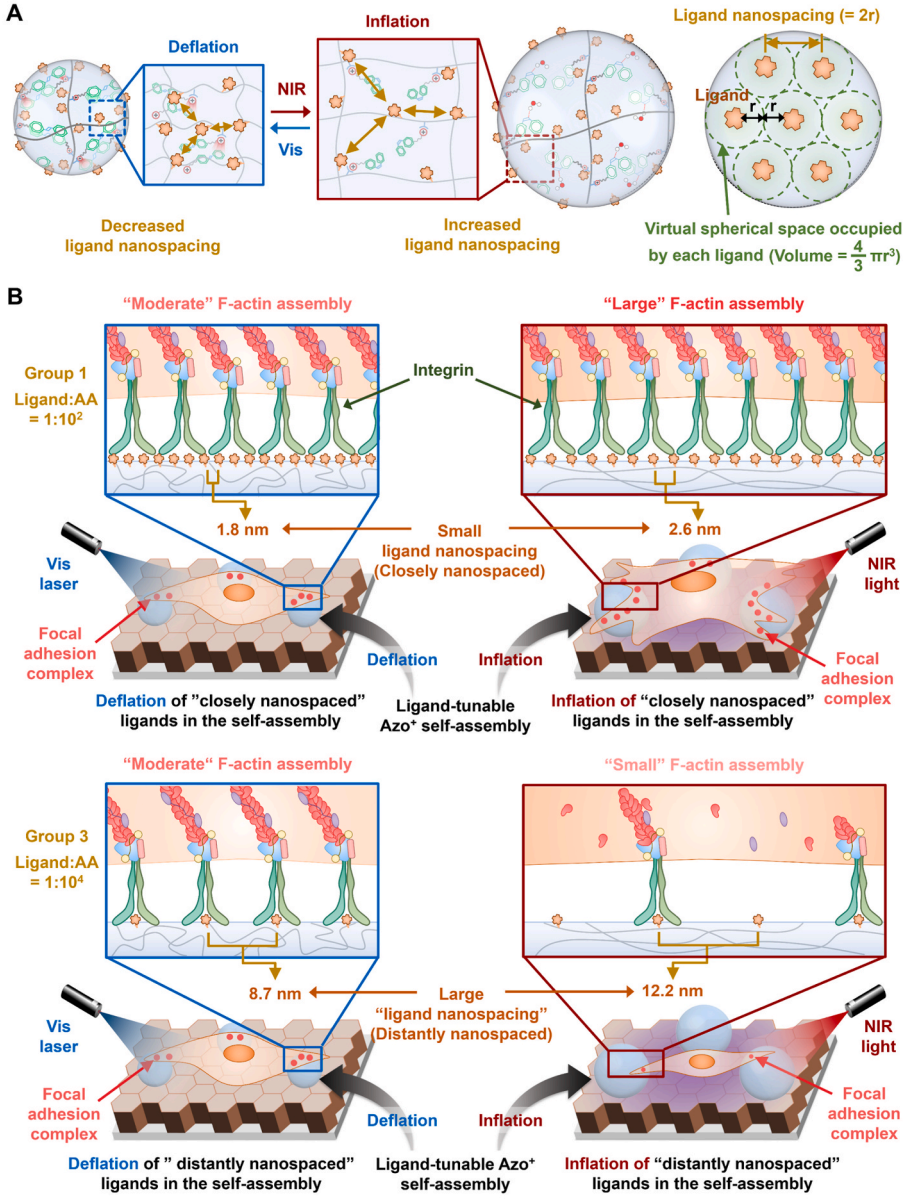


**Fig. 4.** A schematic demonstration of dynamic tuning of ligand nanospacing of ligand-tunable Azo$^+$ self-assemblies upon inflation and deflation that regulates stem cell adhesion. (A) Ligand nanospacing in ligand-tunable Azo$^+$ self-assembly calculated by the diameter of virtual spherical space occupied by each ligand. Inflation of ligand-tunable Azo$^+$ self-assembly via NIR-to-UV light transduction inhibits cation-π interactions that increases ligand nanospacing of ligand-tunable Azo$^+$ self-assembly while maintaining the total number of ligands per self-assembly constant. Contrarily, deflation of ligand-tunable Azo$^+$ self-assembly via Vis light stimulates cation-π interactions that decreases ligand nanospacing of ligand-tunable Azo$^+$ self-assembly. (B) Different trends of stem cell regulation upon inflation and deflation of ligand-tunable Azo$^+$ self-assemblies are observed depending on the ratio of (the number of conjugated ligand):(the number of acrylic acid (AA) units in PAA backbone).

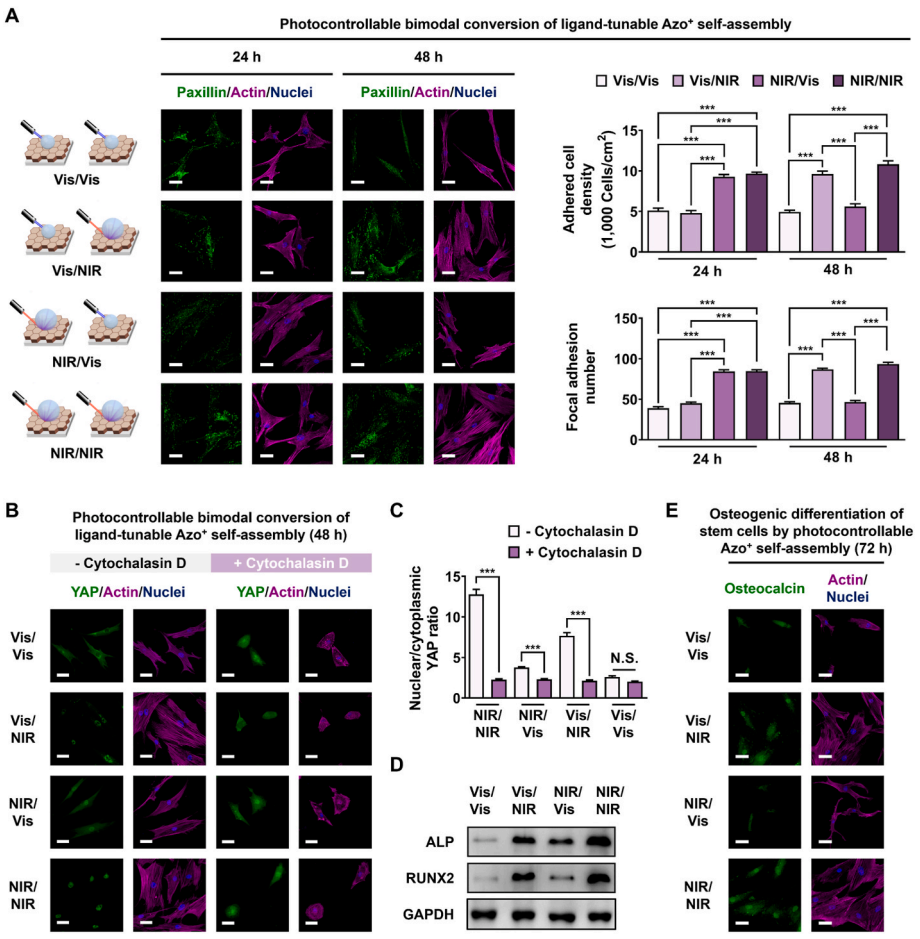


**Fig. 5.** NIR and Vis laser-controlled temporal control of ligand-tunable $Azo^+$ self-assemblies dynamically regulate the focal adhesion-mediated mechanosensing and osteogenic differentiation of stem cells. (A) Immunofluorescence staining for F-actin and nuclei with paxillin after 24 h and 48 h and associated quantification of adhered cell density and focal adhesion number. During stem cell culturing, NIR (1 W/$cm^2$ for 1 min) or Vis (0.2 W/$cm^2$ for 10 min) laser application was replicated or changed at 0 h and 24 h during culturing: i.e., Vis/Vis, Vis/NIR, NIR/Vis, and NIR/NIR groups. Scale bars represent 50 μm. (B) Immunofluorescence staining images for YAP and (C) associated quantification of nuclear/cytoplasmic YAP ratio with or without a specific inhibitor for actin polymerization (cytochalasin D) at 48 h after stem cell seeding. Stem cells were seeded onto ligand-tunable $Azo^+$ self-assemblies with ligand:AA = $1:10^2$ on the UCNT-β-carotene-grafted material. NIR or Vis laser application was replicated ("Vis/Vis" and "NIR/NIR" groups) or changed ("Vis/NIR" and "NIR/Vis" groups changed at 24 h) every 12 h during culturing. Scale bars represent 50 μm. (D) Western blotting images of ALP and RUNX2 with GAPDH and (E) immunofluorescence staining for osteocalcin with F-actin and nuclei at 72 h after stem cell seeding *in vitro*. NIR (1 W/$cm^2$) and Vis (0.2 W/$cm^2$) laser application for 1 min and 10 min, respectively, was replicated ("Vis/Vis" and "NIR/NIR" groups) or changed ("Vis/NIR" and "NIR/Vis" groups changed at 36 h) every 12 h during culturing to analyze stem cell differentiation at 72 h after *in vitro* culturing. Scale bars represent 50 μm. The mean ± standard error represents the data (n = 10). Statistically significant difference is represented as asterisks (***: $p < 0.001$). Statistically non-significant differences are represented as the N.S.

To calculate ligand nanospacing of ligand-tunable $Azo^+$ self-assemblies, we assume that "virtual space occupied by each ligand" exists as spheres in a close contact with another that constitute the total space of each ligand-tunable $Azo^+$ self-assembly (Fig. 4A). We then calculated the ligand nanospacing of ligand-tunable $Azo^+$ self-assembly was estimated to be 1.8 nm and 2.6 nm in deflated and inflated states, respectively, while maintaining the total number of ligands per ligand-tunable $Azo^+$ self-assembly constant. Therefore, both the ligand nanospacing of 1.8 nm and 2.6 nm were likely recognized by cells as if the ligands were saturated and thus continuous. This explains that the inflated state of ligand-tunable $Azo^+$ self-assemblies with ligand:AA = $1:10^2$ (Group 1) presenting higher surface area of "closely nanospaced" ligands significantly promoted integrin binding and stem cell adhesion compared with their deflated state (Fig. 4B, S26, and S27).

Different trends of stem cell regulation upon inflation and deflation of ligand-tunable $Azo^+$ self-assemblies were observed depending on the ratio of ligand:AA. To explore the effect of ligand nanospacing on stem cell adhesion, we used the liganded self-assembly with varying ratio of ligand:AA [ligand:AA = $1:10^2$ (Group 1), ligand:AA = $1:10^3$ (Group 2), ligand:AA = $1:10^4$ (Group 3), and ligand:AA = $1:10^5$ (Group 4)]. We found that higher degree of stem cell adhesion was observed in the inflated state of "closely nanospaced" ligands compared with the deflated state when using the ligand:AA = $1:10^2$ (Group 1). Lower degree of stem cell adhesion is observed in the inflated state compared with the deflated state of "distantly nanospaced" ligands when using the ligand:AA = $1:10^4$ (Group 3). This suggests that the "ligand nanospacing" is the most crucial factor that regulates integrin binding and stem cell adhesion. On the other hand, when using the ligand-tunable $Azo^+$ self-assemblies with ligand:AA = $1:10^3$ (Group 2) and ligand:AA = $1:10^5$ (Group 4), the degrees of stem cell adhesion showed no differences between the inflated state and the deflated state of liganded self-assembly (Figs. S26 and S27). Consequently, to temporally regulate the stem cell by controlling the surface area of "closely spaced" liganded self-assembly, we used the $Azo^+$ self-assembly incorporated with " ligand:

AA = 1:$10^2$ (Group 1)" for this study.

Next, NIR or Vis laser application *in situ* was either replicated ("Vis/Vis" and "NIR/NIR" groups) or changed ("Vis/NIR" and "NIR/Vis" groups changed at 24 h) over 48 h of culturing to explore time-regulated mechanosensing. Similarly, temporal differentiation was examined at 72 h after replicating or changing NIR or Vis laser application at 36 h. During stem cell culturing, NIR or Vis laser application was replicated ("Vis/Vis/Vis" and "NIR/NIR/NIR" groups) or changed ("Vis/NIR/Vis" and "NIR/Vis/NIR" groups) every 24 h to investigate cyclic photocontrollable focal adhesion of stem cells. NIR or Vis laser was applied every 24 h due to the high stability of the *trans*-to-*cis* isomerized state in the *cis*-$Azo^+$-ligand self-assemblies enabling them to persist for 24 h (Fig. S21). Immunofluorescence staining images revealed that the repetition of "NIR"-triggered inflation of liganded self-assemblies ("NIR/NIR" group) or "Vis"-triggered deflation of liganded self-assemblies ("Vis/Vis" group) stimulated or inhibited the focal adhesion (i.e., paxillin clustering) of stem cells, respectively. Remarkably, time-regulated changing of Vis to NIR laser ("Vis/NIR" group) or NIR to Vis laser ("NIR/Vis" group) temporally activates or deactivates stem cell adhesion after their changing, respectively (Fig. 5A and S28). Similarly, continuous application of NIR ("NIR/NIR/NIR") to inflate or Vis ("Vis/Vis/Vis") to deflate the self-assembly facilitates or suppresses the stem cell adhesion, respectively. Additional changing of irradiated wavelength can cyclically regulate the stem cell adhesion, in which temporal changing from Vis to NIR ("NIR/Vis/NIR" group) significantly elevated stem cell adhesion whereas NIR to Vis changing ("Vis/NIR/Vis" group) significantly suppressed stem cell adhesion (Fig. S29).

Furthermore, SEM images and quantification of gold nanoparticles that indicates integrin β1 of stem cell interacting with ligand-tunable $Azo^+$ self-assemblies verified photocontrollable inflation or deflation of liganded self-assemblies promoted or hindered integrin-ligand binding, respectively, that mediated stem cell adhesion (Fig. S30). These findings prove that the time-regulated *in situ* dynamic controlling of ligand-tunable $Azo^+$ self-assemblies by dual-wavelength laser enables remote manipulation of cyclic regulation of stem cell adhesion. These results are different from recent studies of dynamic cell modulation via harmful UV laser [48], light-manipulable static system [52], or self-assembly-based non-controllable system [68,87]. They are also differentiated from recent reports of magnetic field-mediated directional movement of magnetic nanomaterials [32,33,88] or self-assembly-based regulation using strongly acidic harmful conditions [65].

We considered how NIR or Vis laser can independently regulate stem cell adhesion by performing control experiments. To clearly understand which components are necessary for stem cell regulation via NIR and Vis laser-based control of the *in situ* inflation and deflation of ligand-tunable $Azo^+$ self-assemblies on the UCNT (core/shell)-β-carotene-grafted material, several control experiments were conducted. The stem cell adhesion was not facilitated in the absence of ligand-tunable $Azo^+$ self-assemblies, with ligand-tunable $Azo^+$ self-assemblies but without ligand conjugation to PAA or scrambled ligand incorporation (Figs. S31, S32, and S33). This proves that stem cell adhesion was specifically modulated by integrin-ligand binding to the liganded self-assemblies. It has been known that membrane bending energy of cells inhibit cells to adhere on highly curved nanostructured surface [89], which is consistent with the decrease in the curvature upon the inflation of ligand-tunable $Azo^+$ self-assembly. Also, the stiffness of glass substrate is significantly higher than that of the self-assembly. These suggest that the curvature nor stiffness change during inflation and deflation of liganded self-assemblies may not be a dominant regulator for stem cell adhesion. Furthermore, stem cell adhesion was not promoted in the absence of either $NaYF_4$ shell in the UCNTs or β-carotene, thereby proving the need of $NaYF_4$ shell in the UCNTs (core/shell) and β-carotene to synergistically enable specific NIR-to-UV transduction in high photoluminescence intensity (Figs. S34 and S35). We have summarized control groups used for *in vitro* stem cell experiments in Table S2.

### 3.5. NIR and Vis laser temporally regulate focal adhesion-mediated mechanosensing of stem cells and their differentiation via in situ dynamic control of ligand-tunable $Azo^+$ self-assemblies

The inflation and deflation of ligand-tunable $Azo^+$ self-assemblies demonstrated in this study modulate the ligand nanospacing and area of liganded surface involving position changes in dynamic integrin-ligand binding, which regulate mechanosensing signaling and subsequent differentiation of stem cells (e.g., osteogenic differentiation) [6]. In this regard, we explored focal adhesion-mediated mechanosensing and osteogenic differentiation of stem cells upon photocontrolled inflation and deflation of $Azo^+$ self-assembly. Stem cells were cultured on ligand-tunable $Azo^+$ self-assemblies on the UCNT-β-carotene-grafted material. Immunofluorescence staining images with associated quantification reveal that the "NIR" application group had significantly elevated nuclear translocation of the YAP mechanosensor (i.e., a higher nuclear/cytoplasmic YAP immunofluorescence ratio) as well as expression of osteogenic differentiation markers (i.e., a higher nuclear/cytoplasmic RUNX2 immunofluorescence ratio and elevated immunofluorescence intensities of ALP and osteocalcin) compared with the "Vis" application and "No irradiation" groups (Figs. S36 and S37).

Next, NIR or Vis laser application *in situ* was either replicated ("Vis/Vis" and "NIR/NIR" groups) or changed ("Vis/NIR" and "NIR/Vis" groups changed at 24 h) over 48 h of culturing to explore time-regulated mechanosensing. NIR or Vis laser application was also either replicated ("Vis/Vis" and "NIR/NIR" groups) or changed (the "Vis/NIR" and "NIR/Vis" groups changed at 36 h) over 72 h of culturing to explore temporal differentiation. Immunofluorescence staining and western blotting images demonstrate that the replication of NIR laser application ("NIR/NIR" group) significantly augmented the nuclear translocation of YAP and TAZ as well as the expression of RUNX2, ALP, and osteocalcin as compared with those of replicated Vis laser application ("Vis/Vis" group) (Fig. 5B, C, D, and E, S38, S39, and S40). Intriguingly, time-regulated changing of Vis to NIR laser ("Vis/NIR" group) or NIR to Vis laser ("NIR/Vis" group) indicated temporal activation or deactivation after their changing, respectively. Furthermore, time-regulated differentiation of stem cells corresponded to the trend of Dex release (Fig. 3F). In conclusion, *in situ* dynamic regulation to change ligand-tunable $Azo^+$ self-assemblies via tissue-penetrating UV-free NIR and Vis laser application, which modulates the ligand nanospacing and the area of liganded surface, regulates focal adhesion-mediated mechanosensing and resulting differentiation in a time-regulated manner.

Dynamic integrin-ligand binding that occurs in response to the inflation and deflation of ligand-tunable $Azo^+$ self-assemblies can activate phosphorylated focal adhesion kinase (p-FAK) and RhoA associated with cytoskeleton regulation to trigger mechanotransduction and stem cell differentiation [6]. Immunofluorescence staining images illustrate that the expression levels of p-FAK and RhoA in the "Vis/NIR" and "NIR/NIR" groups were more pronounced than those in the "NIR/Vis" and "Vis/Vis" groups (Fig. S41A). RhoA stimulation can activate rho-associated protein kinase (ROCK), thereby inducing actin filament polymerization containing myosin II. Inhibition of actin filament polymerization, myosin II, and ROCK significantly suppressed the nuclear translocation of YAP in the "Vis/NIR" and "NIR/NIR" groups, suggesting the focal adhesion-assisted mechanotransduction of stem cells that occurs after NIR-stimulated inflation of ligand-tunable $Azo^+$ self-assemblies (Fig. 5B and C, S41, and S42). Furthermore, we examined whether the endocytosis of ligand-tunable $Azo^+$ self-assemblies occurs in the presence of stem cell. To fluorescently track the self-assemblies, ligand- and dye-conjugated PAA was synthesized and incorporated into $Azo^+$-(ligand-dye) self-assemblies (Fig. S43). Red-fluorescent live cell dye-stained stem cells were seeded onto the $Azo^+$-(ligand-dye) self-assemblies on the UCNT-grafted material without β-carotene that interferes fluorescence signal of the dye (Fig. S44A). 3-D confocal microscopy fluorescence image with 12 cross-sectioned images along x-axis, and computed Pearson's correlation coefficient

demonstrated that there was no signal overlaps between red-fluorescent cell and green-fluorescent Azo$^+$-(ligand-dye) self-assemblies, confirming that negligible endocytosis of the liganded self-assemblies occurred (Fig. S44). This is consistent with previous reports that cellular uptake efficiency of the particles is extremely low when they exhibit the size larger than 1 μm [90] or are composed of soft materials [91].

### 3.6. Remote manipulation of synergistic stem cell differentiation in vivo via dual-wavelength laser irradiation

As a model for the *in vivo* translation of the regulation in the stem cell focal adhesion, mechanotransduction, and differentiation by tissue-penetrating dual-wavelength (NIR and Vis) laser, we subcutaneously implanted the Dex-loaded ligand-tunable Azo$^+$ self-assemblies on the UCNT-β-carotene-grafted material (robust silicon substrate) into balb/c nude mice. Stem cell regulation was evaluated by injecting them onto the implants followed by either replicating ("Vis/Vis" and "NIR/NIR" groups) or changing ("Vis/NIR" and "NIR/Vis" groups changed at 3 h) NIR (1 W/cm$^2$ for 1 min) or Vis (0.2 W/cm$^2$ for 10 min) laser application to the backs of the mice every 3 h for temporal control of ligand nanospacing, surface area of closely nanospaced liganded surface, and Dex release.

Representative immunofluorescence staining images and subsequent quantification consistently demonstrated that stem cells adhered to the Dex-loaded ligand-tunable Azo$^+$ self-assemblies on the UCNT-β-carotene-grafted material at 6 h post-injection exhibited the following traits: significantly higher adhesion density, focal adhesion, and spreading as well as nuclear translocation of YAP and RUNX2 of human-specific HuNu-positive stem cells in the "Vis/NIR" and "NIR/NIR" groups than those in the "NIR/Vis" and "Vis/Vis" groups (Fig. 6A and B, and S45). Furthermore, immunohistochemical staining of osteocalcin (late marker of osteogenic differentiation) revealed that osteocalcin was highly expressed in the cells at 3 d in the "Vis/NIR" and "NIR/NIR" groups than those in the "NIR/Vis" and "Vis/Vis" groups, thereby confirming

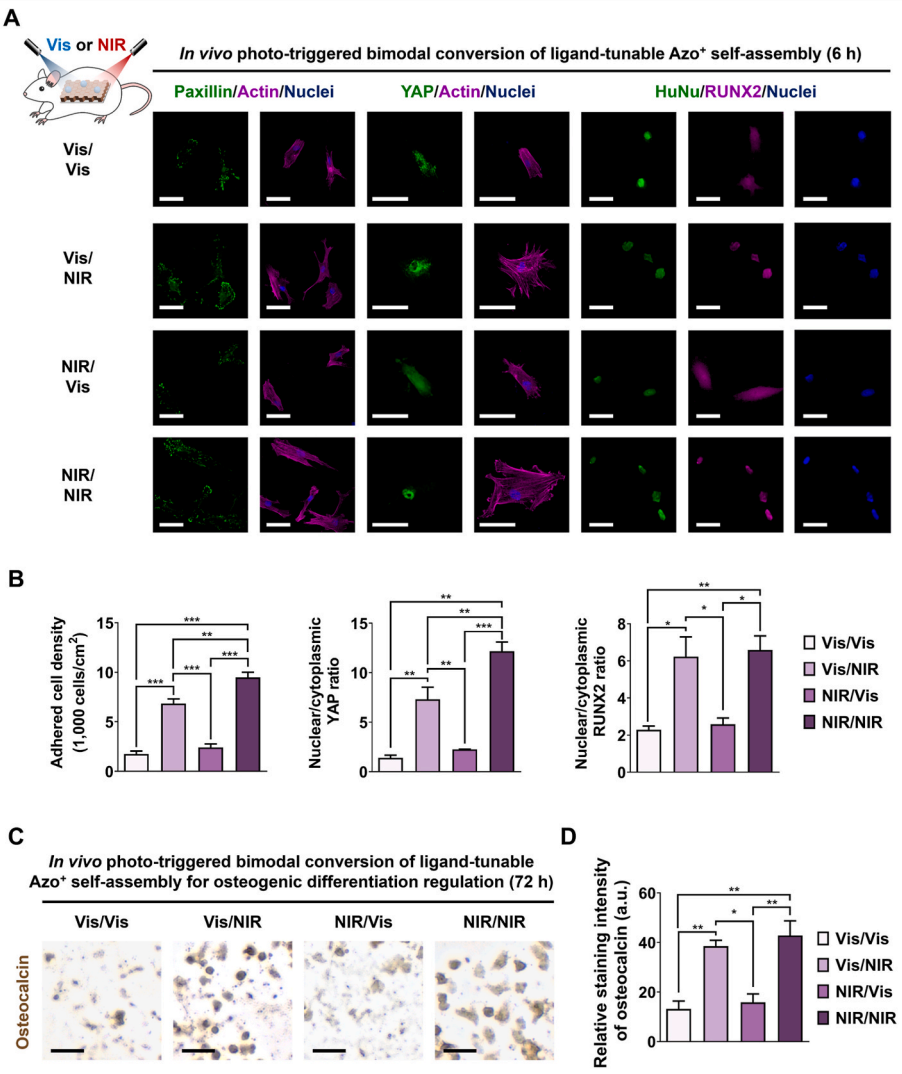


**Fig. 6.** UV-free dual NIR and Vis laser-controlled dynamic conversion of ligand-tunable Azo$^+$ self-assembly for time-regulated osteogenic differentiation of stem cells *in vivo*. (A) Schematic and immunofluorescence staining for paxillin and YAP with F-actin and nuclei and RUNX2 with human specific HuNu and nuclei (B) and associated quantification of adhered cell density, nuclear/cytoplasmic YAP and RUNX2 immunofluorescence ratio of stem cells at 6 h after stem cell injection and subcutaneous implantation *in vivo* followed by replicating or changing NIR and Vis laser application to the backs of mice at 0 and 3 h after implantation. (C) Immunocytochemical staining for osteocalcin at 72 h after stem cell injection and subcutaneous implantation *in vivo* followed by replicating or changing NIR and Vis laser application to the backs of mice at 0 and 36 h after implantation. (D) Associated computation of relative osteocalcin staining intensity using the images shown in (C). Dex-loaded ligand-tunable Azo$^+$ self-assemblies with ligand:AA = 1:10$^2$ on the UCNT-β-carotene-grafted material were used. Scale bars: (A) 50 μm and (C) 100 μm. The mean ± standard error represents the data (n = 10). Statistically significant differences are represented as asterisks (*: $p < 0.05$; **: $p < 0.01$, ***: $p < 0.001$). Statistically non-significant differences are represented as the N.S.

sufficient osteogenic differentiation *in vivo* (Fig. 6C and D). These findings prove that replicated NIR application ("NIR/NIR" group) and time-regulated changing from Vis to NIR laser ("Vis/NIR" group) effectively induced the inflation-mediated increase in liganded surface area and Dex release that synergistically stimulated the focal adhesion-mediated mechanotransduction of stem cells and their differentiation owing to the use of tissue-penetrating UV-free dual-wavelength laser and efficient NIR-to-UV transduction *in vivo*.

Next, we carried out *in vivo* tracking of long-term stability of $Azo^+$-dye self-assemblies on the UCNT-grafted material (Fig. 7). Here, we used the $Azo^+$-dye self-assemblies on the UCNT-grafted material without β-carotene such that the fluorescent dyes in the self-assemblies do not interfere with Vis light absorption by the β-carotene (Fig. 7A). Under NIR laser application, NIR-transduced-Vis light emitted from the UCNTs was transferred to the $Azo^+$-dye self-assemblies and triggered green light fluorescent signal from $Azo^+$-dye self-assemblies that were maintained for 21 d post-implantation and decreased with statistical significance from the 28 d post-implantation, demonstrating long-term tracking of *in vivo* stability of $Azo^+$ -dye self-assemblies (Fig. 7B and S46). We also confirmed the *in vivo* stability of the ligand-tunable $Azo^+$ self-assemblies by examining individual fluorescent-dye-incorporated ligand-tunable $Azo^+$ self-assemblies on the UCNT-β-carotene-grafted material at 6 h after implantation. A similar number of highly stable fluorescent self-assemblies with negligible degradation was present pre-implantation and 6 h post-implantation (Fig. S47). *In vivo* stability of UCNT-β-carotene-grafted material was evaluated by measuring photoluminescence spectra with photoluminescence intensity at 807 nm (distinct photoluminescence peak wavelength) and transduced UV/Vis ratio. The

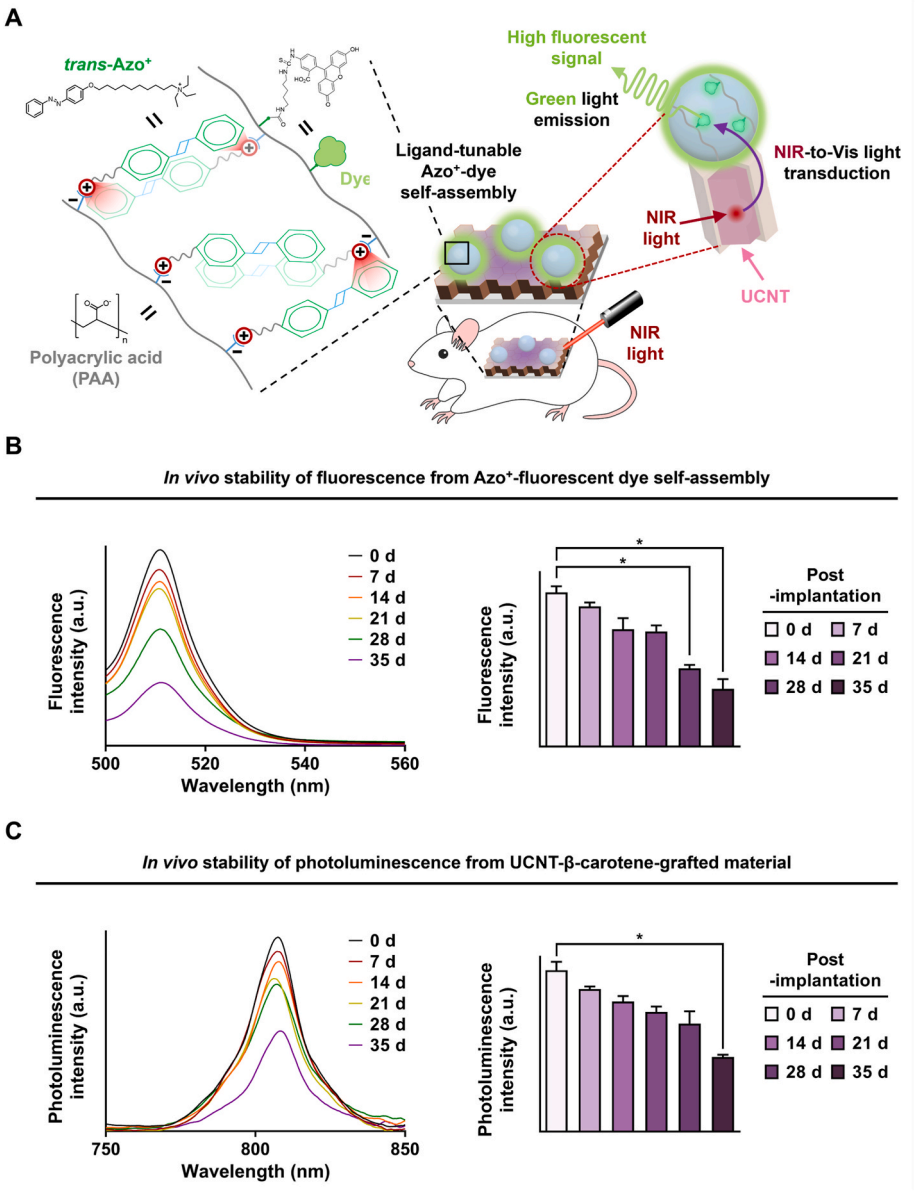


**Fig. 7.** *In vivo* long-term stability of ligand-tunable $Azo^+$ self-assemblies and UCNT-β-carotene-grafted material. (A) Schematic illustration of fluorescent imaging of ligand-tunable $Azo^+$-dye self-assemblies on the UCNT-grafted material *in vivo*. Ligand-tunable $Azo^+$-dye self-assembly containing green-fluorescent dye-conjugated PAA and $Azo^+$ are anchored to the UCNT-grafted material surface. Under NIR laser application, NIR-upconverted-Vis light from UCNT-grafted material is absorbed by ligand-tunable $Azo^+$ self-assembly. Sequentially, absorbed Vis light activates green light fluorescence dye. (B) Fluorescence spectra and fluorescence intensity at 511 nm under an application of 980 nm NIR laser at 0 d, 7 d, 14 d, 21 d, 28 d, and 35 d post-implantation. (C) Photoluminescence spectra and photoluminescence intensity at 807 nm under an application of 980 nm NIR laser at 0 d, 7 d, 14 d, 21 d, 28 d, and 35 d post-implantation. The mean ± standard error represents the data (n = 3). Statistically significant differences are represented as asterisks (*: $p < 0.05$). Statistically non-significant differences are represented as the N.S.

results showed maintained photoluminescence intensity at 807 nm for 28 d post-implantation and nearly constant values of UV/Vis ratio for 7 d post-implantation, thereby confirming *in vivo* stability of UCNT-β-carotene-grafted material (Fig. 7C and S48).

We found that the implanted ligand-tunable $Azo^+$ self-assemblies on the UCNT-β-carotene-grafted material along with NIR and Vis laser irradiation *in vivo* exhibited both locally and systemically non-toxicity in a good agreement with the long-term non-toxicity of azobenzene derivatives, PAA polyanions, and UCNTs reported in previous studies (Fig. S49) [92,93]. This presents our material with bright prospects for safe, dynamic, and multimodal control of ligand nanospacing, surface area of closely nanospaced liganded surface, and drug release for potential applications [94].

## 4. Conclusions

In summary, we demonstrated UV-free laser-based remote manipulation of liganded self-assembly that was applied for stem cell regulation *in vivo*. The UV-free laser-based control that can be spatially localized was enabled by developing UCNTs with core/shell nanostructures and β-carotene to facilitate predominant NIR-to-UV transduction over NIR-to-Vis transduction with high photoluminescence intensity. NIR or Vis laser-mediated photoisomerization of $Azo^+$ molecules modulated ligand nanospacing and surface area of closely nanospaced liganded surface via tuning of cation-π interactions, which enabled cyclic control of stem cell adhesion and regulated their focal adhesion and differentiation synergistically with released molecules both *in vitro* and *in vivo*. Versatile use of bioactive ligands and molecule loading as well as tunability of the functional groups adjacent to the aromatic rings in the azobenzene derivative can diversify the choice of tissue-penetrating laser wavelength for stem cell regulation toward realizing regenerative therapies. Owing to dynamic controllability of self-assembly, liganded self-assembly can be utilized for organoid *in vitro* as drug screening platform and on-demand drug delivery system for sustained cancer therapy, immunotherapy, and tissue regeneration therapy for *in vivo* application.

## Ethics approval and consent to participate

All the procedures for handling animals were conducted under the Institutional Animal Care and Use Committee at Korea University (Permit No. KOREA-2021-0006).

## CRediT authorship contribution statement

**Sungkyu Lee:** Data curation, Formal analysis, Investigation, Writing – original draft. **Jounghyun Yoo:** Formal analysis, Methodology, Resources, Writing – original draft. **Gunhyu Bae:** Data curation, Formal analysis, Investigation, Visualization. **Ramar Thangam:** Investigation, Methodology, Validation. **Jeongyun Heo:** Data curation, Methodology, Resources. **Jung Yeon Park:** Investigation, Software. **Honghwan Choi:** Investigation, Resources. **Chowon Kim:** Investigation, Visualization. **Jusung An:** Resources, Validation. **Jungryun Kim:** Resources, Validation. **Kwang Rok Mun:** Formal analysis, Resources. **Seungyong Shin:** Formal analysis, Resources. **Kunyu Zhang:** Data curation, Validation. **Pengchao Zhao:** Data curation, Validation. **Yuri Kim:** Investigation, Writing – original draft. **Nayeon Kang:** Investigation, Visualization. **Seong-Beom Han:** Data curation, Visualization. **Dahee Kim:** Data curation, Investigation. **Jiwon Yoon:** Investigation, Resources. **Misun Kang:** Investigation, Resources. **Jihwan Kim:** Investigation, Resources. **Letao Yang:** Data curation, Validation. **Solmaz Karamikamkar:** Data curation, Validation. **Jinjoo Kim:** Data curation, Methodology. **Yangzhi Zhu:** Methodology, Validation. **Alireza Hassani Najafabadi:** Data curation, Methodology. **Guosheng Song:** Data curation, Formal analysis. **Dong-Hwee Kim:** Investigation, Visualization. **Ki-Bum Lee:** Data curation, Validation. **Soong Ju Oh:** Data curation, Validation. **Hyun-Do Jung:** Resources, Validation. **Hyun-Cheol Song:** Resources, Validation. **Woo Young Jang:** Investigation, Resources. **Liming Bian:** Methodology, Resources. **Zhiqin Chu:** Data curation, Methodology. **Juyoung Yoon:** Investigation, Software. **Jong Seung Kim:** Formal analysis, Resources. **Yu Shrike Zhang:** Data curation, Validation. **Yongju Kim:** Investigation, Software, Visualization. **Ho Seong Jang:** Data curation, Funding acquisition, Methodology, Resources, Supervision. **Sehoon Kim:** Conceptualization, Funding acquisition, Project administration, Resources, Supervision. **Heemin Kang:** Conceptualization, Funding acquisition, Project administration, Supervision, Writing – review & editing.

## Declaration of competing interest

The authors declare that they have no known competing financial interests or personal relationships that could have appeared to influence the work reported in this paper.

## Acknowledgements

This work was supported by the National Research Foundation of Korea (NRF) grant funded by the Korean government (MSIT) (No. RS-2023-00208427, 2021R1I1A1A01046207, 2021R1A2C2005418, 2022R1A2C2005943, and 2022M3H4A1A03076638). This research was supported by Basic Science Research Program through the National Research Foundation of Korea (NRF) funded by the Ministry of Education (No. RS-2023-00271399 and RS-2023-00275654). This work was also supported by a Korea University Grant and KIST intramural program. HAADF-STEM was conducted with the support of the Seoul center in Korea Basic Science Institute (KBSI).

## Appendix A. Supplementary data

Supplementary data to this article can be found online at https://doi.org/10.1016/j.bioactmat.2023.12.011.

## References

[1] J.K. Mouw, G. Ou, V.M. Weaver, Extracellular matrix assembly: a multiscale deconstruction, Nat. Rev. Mol. Cell Biol. 15 (2014) 771–785, https://doi.org/10.1038/nrm3902.
[2] M. Carlsson, P. Cain, C. Holmqvist, F. Stahlberg, S. Lundback, H. Arheden, Total heart volume variation throughout the cardiac cycle in humans, Am. J. Physiol. Heart Circ. Physiol. 287 (2004) H243–H250, https://doi.org/10.1152/ajpheart.01125.2003.
[3] G.M. Thornton, C.B. Frank, N.G. Shrive, Ligament creep behavior can be predicted from stress relaxation by incorporating fiber recruitment, J. Rheol. 45 (2001) 493–507, https://doi.org/10.1122/1.1343877.
[4] D.E. Carney, C.E. Bredenberg, H.J. Schiller, A.L. Picone, U.G. McCann, L.A. Gatto, G. Bailey, M. Fillinger, G.F. Nieman, The mechanism of lung volume change during mechanical ventilation, Am. J. Resp. Crit. Care 160 (1999) 1697–1702, https://doi.org/10.1164/ajrccm.160.5.9812031.
[5] S.I. Rapoport, M. Hori, I. Klatzo, Reversible osmotic opening of the blood-brain barrier, Science 173 (1971) 1026–1028, https://doi.org/10.1126/science.173.4001.1026.
[6] K.H. Vining, D.J. Mooney, Mechanical forces direct stem cell behaviour in development and regeneration, Nat. Rev. Mol. Cell Biol. 18 (2017) 728–742, https://doi.org/10.1038/nrm.2017.108.
[7] D.W. Zhou, M.A. Fernández-Yagüe, E.N. Holland, A.F. García, N.S. Castro, E. B. O'Neill, J. Eyckmans, C.S. Chen, J. Fu, D.D. Schlaepfer, Force-FAK signaling coupling at individual focal adhesions coordinates mechanosensing and microtissue repair, Nat. Commun. 12 (2021) 1–13, https://doi.org/10.1038/s41467-021-22602-5.
[8] R. Glazier, J.M. Brockman, E. Bartle, A.L. Mattheyses, O. Destaing, K. Salaita, DNA mechanotechnology reveals that integrin receptors apply pN forces in podosomes on fluid substrates, Nat. Commun. 10 (2019) 1–13, https://doi.org/10.1038/s41467-019-12304-4.
[9] N. Heitman, R. Sennett, K.-W. Mok, N. Saxena, D. Srivastava, P. Martino, L. Grisanti, Z. Wang, A. Ma'ayan, P. Rompolas, Dermal sheath contraction powers stem cell niche relocation during hair cycle regression, Science 367 (2020) 161–166, https://doi.org/10.1126/science.aax9131.
[10] Y. Jin, D. Shahriari, E.J. Jeon, S. Park, Y.S. Choi, J. Back, H. Lee, P. Anikeeva, S. W. Cho, Functional skeletal muscle regeneration with thermally drawn porous fibers and reprogrammed muscle progenitors for volumetric muscle injury, Adv. Mater. 33 (2021), 2007946, https://doi.org/10.1002/adma.202007946.

[11] M. Yang, Q. Li, L. Sheng, H. Li, R. Weng, T. Zan, Bone marrow–derived mesenchymal stem cells transplantation accelerates tissue expansion by promoting skin regeneration during expansion, Ann. Surg. 253 (2011) 202–209, https://doi.org/10.1097/SLA.0b013e3181f9ba1ah.

[12] H.S. Sohn, J.W. Choi, J. Jhun, S.P. Kwon, M. Jung, S. Yong, H.S. Na, J.-H. Kim, M.-L. Cho, B.-S. Kim, Tolerogenic nanoparticles induce type II collagen–specific regulatory T cells and ameliorate osteoarthritis, Sci. Adv. 8 (2022), eabo5284, https://doi.org/10.1126/sciadv.abo5284.

[13] M. Pei, Y.A. Pei, S. Zhou, E. Mikaeiliagah, C. Erickson, B. Giertych, H. Akhter, L. Wang, A. Stewart, J. Parenti, B. Wang, S. Wen, S. Sim, E. Quenneville, K. C. Hansen, S. Frisch, G. Hu, Matrix from urine stem cells boosts tissue-specific stem cell mediated functional cartilage reconstruction, Bioact. Mater. 23 (2023) 353–367, https://doi.org/10.1016/j.bioactmat.2022.11.012.

[14] L. Zhou, J. Xu, A. Schwab, W. Tong, J. Xu, L. Zheng, Y. Li, Z. Li, S. Xu, Z. Chen, L. Zou, X. Zhao, G.J.V.M.v. Osch, C. Wen, L. Qin, Engineered biochemical cues of regenerative biomaterials to enhance endogenous stem/progenitor cells (ESPCs)-mediated articular cartilage repair, Bioact. Mater. 26 (2023) 490–512, https://doi.org/10.1016/j.bioactmat.2023.03.008.

[15] M. Yu, D. Luo, J. Qiao, J. Guo, D. He, S. Jin, L. Tang, Y. Wang, X. Shi, J. Mao, S. Cui, Y. Fu, Z. Li, D. Liu, T. Zhang, C. Zhang, Z. Li, Y. Zhou, Y. Liu, A hierarchical bilayer architecture for complex tissue regeneration, Bioact. Mater. 10 (2022) 93–106, https://doi.org/10.1016/j.bioactmat.2021.08.024.

[16] Q. Sun, Y. Hou, Z. Chu, Q. Wei, Soft overcomes the hard: flexible materials adapt to cell adhesion to promote cell mechanotransduction, Bioact. Mater. 10 (2022) 397–404, https://doi.org/10.1016/j.bioactmat.2021.08.026.

[17] M.J. Dalby, N. Gadegaard, R.O. Oreffo, Harnessing nanotopography and integrin–matrix interactions to influence stem cell fate, Nat. Mater. 13 (2014) 558–569, https://doi.org/10.1038/nmat3980.

[18] J. Li, X. Jiang, H. Li, M. Gelinsky, Z. Gu, Tailoring materials for modulation of macrophage fate, Adv. Mater. 33 (2021), 2004172, https://doi.org/10.1002/adma.202004172.

[19] H.Y. Kim, T.J. Kim, L. Kang, Y.-J. Kim, M.K. Kang, J. Kim, J.H. Ryu, T. Hyeon, B.-W. Yoon, S.-B. Ko, Mesenchymal stem cell-derived magnetic extracellular nanovesicles for targeting and treatment of ischemic stroke, Biomaterials 243 (2020), 119942, https://doi.org/10.1016/j.biomaterials.2020.119942.

[20] H. Jeong, W. Park, D.-H. Kim, K. Na, Dynamic nanoassemblies of nanomaterials for cancer photomedicine, Adv. Drug Deliv. Rev. 177 (2021), 113954, https://doi.org/10.1016/j.addr.2021.113954.

[21] J. Li, F. Han, J. Ma, H. Wang, J. Pan, G. Yang, H. Zhao, J. Zhao, J. Liu, Z. Liu, Targeting endogenous hydrogen peroxide at bone defects promotes bone repair, Adv. Funct. Mater. 32 (2022), 2111208, https://doi.org/10.1002/adfm.202111208.

[22] J. Zhu, H. Zhou, E.M. Gerhard, S. Zhang, F.I. Parra Rodriguez, T. Pan, H. Yang, Y. Lin, J. Yang, H. Cheng, Smart bioadhesives for wound healing and closure, Bioact. Mater. 19 (2023) 360–375, https://doi.org/10.1016/j.bioactmat.2022.04.02.

[23] M. Wen, N. Yu, S. Wu, M. Huang, P. Qiu, Q. Ren, M. Zhu, Z. Chen, On-demand assembly of polymeric nanoparticles for longer-blood-circulation and disassembly in tumor for boosting sonodynamic therapy, Bioact. Mater. 18 (2022) 242–253, https://doi.org/10.1016/j.bioactmat.2022.03.009.

[24] Y. He, F. Li, P. Jiang, F. Cai, Q. Lin, M. Zhou, H. Liu, F. Yan, Remote control of the recruitment and capture of endogenous stem cells by ultrasound for in situ repair of bone defects, Bioact. Mater. 21 (2023) 223–238, https://doi.org/10.1016/j.bioactmat.2022.08.012.

[25] W. Zhao, C. Hu, T. Xu, In vivo bioprinting: broadening the therapeutic horizon for tissue injuries, Bioact. Mater. 25 (2023) 201–222, https://doi.org/10.1016/j.bioactmat.2023.01.018.

[26] M.J. Ko, H. Hong, H. Choi, H. Kang, D.-H. Kim, Multifunctional magnetic nanoparticles for dynamic imaging and therapy, Adv. NanoBiomed Res. 2 (2022), 2200053, https://doi.org/10.1002/anbr.202200053.

[27] Y. Shu, M. Ma, X. Pan, M. Shafiq, H. Yu, H. Chen, Cobalt protoporphyrin-induced nano-self-assembly for CT imaging, magnetic-guidance, and antioxidative protection of stem cells in pulmonary fibrosis treatment, Bioact. Mater. 21 (2023) 129–141, https://doi.org/10.1016/j.bioactmat.2022.08.008.

[28] Y. Zhang, J. Li, P. Habibovic, Magnetically responsive nanofibrous ceramic scaffolds for on-demand motion and drug delivery, Bioact. Mater. 15 (2022) 372–381, https://doi.org/10.1016/j.bioactmat.2022.02.028.

[29] Y. Shou, L. Liu, Q. Liu, Z. Le, K.L. Lee, H. Li, X. Li, D.Z. Koh, Y. Wang, T.M. Liu, Z. Yang, C.T. Lim, C. Cheung, A. Tay, Mechano-responsive hydrogel for direct stem cell manufacturing to therapy, Bioact. Mater. 24 (2023) 387–400, https://doi.org/10.1016/j.bioactmat.2022.12.019.

[30] C. Gao, Z. Zeng, S. Peng, C. Shuai, Magnetostrictive alloys: promising materials for biomedical applications, Bioact. Mater. 8 (2022) 177–195, https://doi.org/10.1016/j.bioactmat.2021.06.025.

[31] J.-u. Lee, W. Shin, Y. Lim, J. Kim, W.R. Kim, H. Kim, J.-H. Lee, J. Cheon, Non-contact long-range magnetic stimulation of mechanosensitive ion channels in freely moving animals, Nat. Mater. 20 (2021) 1029–1036, https://doi.org/10.1038/s41563-020-00896-y.

[32] Y. Kim, H.J. Jung, Y. Lee, S. Koo, R. Thangam, W.Y. Jang, S.Y. Kim, S. Park, S. Lee, G. Bae, K.D. Patel, Q. Wei, K.-B. Lee, R. Paulmurugan, W.K. Jeong, T. Hyeon, D. Kim, H. Kang, Manipulating nanoparticle aggregates regulates receptor–ligand binding in macrophages, J. Am. Chem. Soc. 144 (2022) 5769–5783, https://doi.org/10.1021/jacs.1c08861.

[33] Y. Kim, T.M. Koo, R. Thangam, M.S. Kim, W.Y. Jang, N. Kang, S. Min, S.Y. Kim, L. Yang, H. Hong, H.J. Jung, E.K. Koh, K.D. Patel, S. Lee, H.E. Fu, Y.S. Jeon, B. C. Park, S.Y. Kim, S. Park, J. Lee, L. Gu, D.-H. Kim, T.-H. Kim, K.-B. Lee, W. K. Jeong, R. Paulmurugan, Y.K. Kim, H. Kang, Submolecular ligand size and spacing for cell adhesion, Adv. Mater. 34 (2022), 2110340, https://doi.org/10.1002/adma.202110340.

[34] S. Yan, K. Hu, M. Zhang, J. Sheng, X. Xu, S. Tang, Y. Li, S. Yang, G. Si, Y. Mao, Y. Zhang, F. Zhang, N. Gu, Extracellular magnetic labeling of biomimetic hydrogel-induced human mesenchymal stem cell spheroids with ferumoxytol for MRI tracking, Bioact. Mater. 19 (2023) 418–428, https://doi.org/10.1016/j.bioactmat.2022.04.024.

[35] E. Georgas, M. Yuan, J. Chen, Y. Wang, Y.X. Qin, Bioactive superparamagnetic iron oxide-gold nanoparticles regulated by a dynamic magnetic field induce neuronal Ca(2+) influx and differentiation, Bioact. Mater. 26 (2023) 478–489, https://doi.org/10.1016/j.bioactmat.2023.01.007.

[36] C. Zhou, C. Wang, K. Xu, Z. Niu, S. Zou, D. Zhang, Z. Qian, J. Liao, J. Xie, Hydrogel platform with tunable stiffness based on magnetic nanoparticles cross-linked GelMA for cartilage regeneration and its intrinsic biomechanism, Bioact. Mater. 25 (2023) 615–628, https://doi.org/10.1016/j.bioactmat.2022.07.013.

[37] S.Y. Kim, R. Thangam, N.Y. Kang, H. Hong, C. Kim, S.K.Y. Lee, S. Son, H.J. Lee, K. R. Tag, S.H. Min, D. Jeong, J. Hwang, K. Kim, D. Kim, Y. Kim, J. Joo, B.H. Kim, Y. Z. Zhu, S.G. Park, H.C. Song, W.J. Sun, J.P. Ahn, W.Y. Jang, R. Paulmurugan, H. K. Kim, J.S. Kim, H. Kang, Modulation of macrophages by in situ ligand bridging, Adv. Funct. Mater. 33 (2023), 2215166, https://doi.org/10.1002/adfm.202215166.

[38] R. Thangam, S.Y. Kim, N. Kang, H. Hong, H.J. Lee, S. Lee, D. Jeong, K.R. Tag, K. Kim, Y.Z. Zhu, W.J. Sun, H.J. Kim, S.W. Cho, J.P. Ahn, W.Y. Jang, J.S. Kim, R. Paulmurugan, A. Khademhosseini, H.K. Kim, H. Kang, Ligand coupling and decoupling modulates stem cell fate, Adv. Funct. Mater. 33 (2023), 2206673, https://doi.org/10.1002/adfm.202206673.

[39] Y. Luo, B. Li, X. Liu, Y. Zheng, E. Wang, Z. Li, Z. Cui, Y. Liang, S. Zhu, S. Wu, Simultaneously enhancing the photocatalytic and photothermal effect of NH(2)-MIL-125-GO-Pt ternary heterojunction for rapid therapy of bacteria-infected wounds, Bioact. Mater 18 (2022) 421–432, https://doi.org/10.1016/j.bioactmat.2022.03.035.

[40] N.K. Pandey, W. Xiong, L. Wang, W. Chen, B. Bui, J. Yang, E. Amador, M. Chen, C. Xing, A.A. Athavale, Y. Hao, W. Feizi, L. Lumata, Aggregation-induced emission luminogens for highly effective microwave dynamic therapy, Bioact. Mater. 7 (2022) 112–125, https://doi.org/10.1016/j.bioactmat.2021.05.031.

[41] Y. Qu, K. Lu, Y. Zheng, C. Huang, G. Wang, Y. Zhang, Q. Yu, Photothermal scaffolds/surfaces for regulation of cell behaviors, Bioact. Mater. 8 (2022) 449–477, https://doi.org/10.1016/j.bioactmat.2021.05.052.

[42] C. Wang, Y. Zeng, K.F. Chen, J. Lin, Q. Yuan, X. Jiang, G. Wu, F. Wang, Y.G. Jia, W. Li, A self-monitoring microneedle patch for light-controlled synergistic treatment of melanoma, Bioact. Mater. 27 (2023) 58–71, https://doi.org/10.1016/j.bioactmat.2023.03.016.

[43] Y. Kim, H. Choi, J.E. Shin, G. Bae, R. Thangam, H. Kang, Remote active control of nanoengineered materials for dynamic nanobiomedical engineering, View 1 (2020), 20200029, https://doi.org/10.1002/VIW.20200029.

[44] W. Li, Z. Yan, J. Ren, X. Qu, Manipulating cell fate: dynamic control of cell behaviors on functional platforms, Chem. Soc. Rev. 47 (2018) 8639–8684, https://doi.org/10.1039/C8CS00053K.

[45] M.J. Ko, W. Yoo, S. Min, Y.S. Zhang, J. Joo, H. Kang, D.-H. Kim, Photonic control of image-guided ferroptosis cancer nanomedicine, Coord. Chem. Rev. 500 (2023), 215532, https://doi.org/10.1016/j.ccr.2023.215532.

[46] F.A. Jerca, V.V. Jerca, R. Hoogenboom, Advances and opportunities in the exciting world of azobenzenes, Nat. Rev. Chem 6 (2022) 51–69, https://doi.org/10.1038/s41570-021-00334-w.

[47] L.F. Kadem, K.G. Suana, M. Holz, W. Wang, H. Westerhaus, R. Herges, C. Selhuber-Unkel, High-frequency mechanostimulation of cell adhesion, Angew. Chem. Int. Ed. 129 (2017) 231–235, https://doi.org/10.1002/anie.201609483.

[48] T.T. Lee, J.R. García, J.I. Paez, A. Singh, E.A. Phelps, S. Weis, Z. Shafiq, A. Shekaran, A. Del Campo, A.J. García, Light-triggered in vivo activation of adhesive peptides regulates cell adhesion, inflammation and vascularization of biomaterials, Nat. Mater. 14 (2015) 352–360, https://doi.org/10.1038/nmat4157.

[49] S. Wu, H.J. Butt, Near-infrared-sensitive materials based on upconverting nanoparticles, Adv. Mater. 28 (2016) 1208–1226, https://doi.org/10.1002/adma.201502843.

[50] Y. Wu, J. Xu, X. Qin, J. Xu, X. Liu, Dynamic upconversion multicolour editing enabled by molecule-assisted opto-electrochemical modulation, Nat. Commun. 12 (2021) 1–7, https://doi.org/10.1038/s41467-021-22387-7.

[51] Z. Chu, T. Tian, Z. Tao, J. Yang, B. Chen, H. Chen, W. Wang, P. Yin, X. Xia, H. Wang, H. Qian, Upconversion nanoparticles@AgBiS(2) core-shell nanoparticles with cancer-cell-specific cytotoxicity for combined photothermal and photodynamic therapy of cancers, Bioact. Mater. 17 (2022) 71–80, https://doi.org/10.1016/j.bioactmat.2022.01.010.

[52] H. Kang, K.Y. Zhang, Q. Pan, S.E. Lin, D.S.H. Wong, J.M. Li, W.Y.W. Lee, B.G. Yang, F.X. Han, G. Li, B. Li, L.M. Bian, Remote control of intracellular calcium using upconversion nanotransducers regulates stem cell differentiation in vivo, Adv. Funct. Mater. 28 (2018), 1802642, https://doi.org/10.1002/adfm.201802642.

[53] P. Choo, T. Liu, T.W. Odom, Nanoparticle shape determines dynamics of targeting nanoconstructs on cell membranes, J. Am. Chem. Soc. 143 (2021) 4550–4555, https://doi.org/10.1021/jacs.1c00850.

[54] Z. Zhao, M. Li, J. Zeng, L. Huo, K. Liu, R. Wei, K. Ni, J. Gao, Recent advances in engineering iron oxide nanoparticles for effective magnetic resonance imaging, Bioact. Mater. 12 (2022) 214–245, https://doi.org/10.1016/j.bioactmat.2021.10.014.

[55] X.H. Cheng, P.P. Sun, N. Zhang, S.J. Zhou, X. Xin, Self-assembly of silver nanoclusters and phthalic acid into hollow tubes as a superior sensor for Fe, J. Mol. Liq. 323 (2021), 115032, https://doi.org/10.1016/j.molliq.2020.115032.
[56] Y.T. Bi, Z. Wang, T. Liu, D. Sun, N. Godbert, H.G. Li, J.C. Hao, X. Xin, Supramolecular chirality from hierarchical self-assembly of atomically precise silver nanoclusters induced by secondary metal coordination, ACS Nano 15 (2021) 15910–15919, https://doi.org/10.1021/acsnano.1c03824.
[57] S. Lee, M.S. Kim, K.D. Patel, H. Choi, R. Thangam, J. Yoon, T.M. Koo, H.J. Jung, S. Min, G. Bae, Y. Kim, S.B. Han, N. Kang, M. Kim, N. Li, H.E. Fu, Y.S. Jeon, J. J. Song, D.H. Kim, S. Park, J.W. Choi, R. Paulmurugan, Y.C. Kang, H. Lee, Q. Wei, V.P. Dravid, K.B. Lee, Y.K. Kim, H. Kang, Magnetic control and real-time monitoring of stem cell differentiation by the ligand nanoassembly, Small 17 (2021), 2102892, https://doi.org/10.1002/smll.202102892.
[58] C. Chen, Y. Wang, H. Zhang, H. Zhang, W. Dong, W. Sun, Y. Zhao, Responsive and self-healing structural color supramolecular hydrogel patch for diabetic wound treatment, Bioact. Mater. 15 (2022) 194–202, https://doi.org/10.1016/j.bioactmat.2021.11.037.
[59] L. Chen, J. Deng, A. Yu, Y. Hu, B. Jin, P. Du, J. Zhou, L. Lei, Y. Wang, S. Vakal, X. Li, Drug-peptide supramolecular hydrogel boosting transcorneal permeability and pharmacological activity via ligand-receptor interaction, Bioact. Mater. 10 (2022) 420–429, https://doi.org/10.1016/j.bioactmat.2021.09.006.
[60] R. Haghniaz, H.J. Kim, H. Montazerian, A. Baidya, M. Tavafoghi, Y. Chen, Y. Zhu, S. Karamikamkar, A. Sheikhi, A. Khademhosseini, Tissue adhesive hemostatic microneedle arrays for rapid hemorrhage treatment, Bioact. Mater. 23 (2023) 314–327, https://doi.org/10.1016/j.bioactmat.2022.08.017.
[61] L. Ren, Y. Gao, Y. Cheng, A manganese (II)-based coordinative dendrimer with robust efficiency in intracellular peptide delivery, Bioact, Mater 9 (2022) 44–53, https://doi.org/10.1016/j.bioactmat.2021.08.006.
[62] H. Wu, Y. Shang, W. Sun, X. Ouyang, W. Zhou, J. Lu, S. Yang, W. Wei, X. Yao, X. Wang, X. Zhang, Y. Chen, Q. He, Z. Yang, H. Ouyang, Seamless and early gap healing of osteochondral defects by autologous mosaicplasty combined with bioactive supramolecular nanofiber-enabled gelatin methacryloyl (BSN-GelMA) hydrogel, Bioact. Mater. 19 (2023) 88–102, https://doi.org/10.1016/j.bioactmat.2022.03.038.
[63] C. Lu, C. Zhang, P. Wang, Y. Zhao, Y. Yang, Y.J. Wang, H.F. Yuan, S.L. Qu, X. B. Zhang, G.S. Song, K.Y. Pu, Light-free generation of singlet oxygen through manganese-thiophene nanosystems for pH-responsive chemiluminescence imaging and tumor therapy, Chem 6 (2020) 2314–2334, https://doi.org/10.1016/j.chempr.2020.06.024.
[64] Y. Sun, X. Li, M. Zhao, Y. Chen, Y. Xu, K. Wang, S. Bian, Q. Jiang, Y. Fan, X. Zhang, Bioinspired supramolecular nanofiber hydrogel through self-assembly of biphenyl-tripeptide for tissue engineering, Bioact. Mater. 8 (2022) 396–408, https://doi.org/10.1016/j.bioactmat.2021.05.054.
[65] C. Li, A. Iscen, H. Sai, K. Sato, N.A. Sather, S.M. Chin, Z. Álvarez, L.C. Palmer, G. C. Schatz, S.I. Stupp, Supramolecular–covalent hybrid polymers for light-activated mechanical actuation, Nat. Mater. 19 (2020) 900–909, https://doi.org/10.1038/s41563-020-0707-7.
[66] S.J. Zhou, K. Sheng, N. Zhang, S.D. Yuan, N. Feng, Y.X. Song, J.F. Geng, X. Xin, Reversible demulsification and emulsification of surfactant emulsions regulated by light-responsive azo functionalized copper nanoclusters, J. Mol. Liq. 367 (2022), 120384, https://doi.org/10.1016/j.molliq.2022.120384.
[67] S.J. Zhou, S.S. Zhang, H.P. Li, D. Sun, J.Z. Zhang, X. Xin, Solvent-induced self-assembly of copper nanoclusters for white light emitting diodes, ACS Appl. Nano Mater. 4 (2021) 10911–10920, https://doi.org/10.1021/acsanm.1c02374.
[68] S. Chagri, D.Y. Ng, T. Weil, Designing bioresponsive nanomaterials for intracellular self-assembly, Nat. Rev. Chem 6 (2022) 320–338, https://doi.org/10.1038/s41570-022-00373-x.
[69] Z. Yang, B. Wang, W. Liu, X. Li, K. Liang, Z. Fan, J.J. Li, Y. Niu, Z. He, H. Li, D. Wang, J. Lin, Y. Du, J. Lin, D. Xing, In situ self-assembled organoid for osteochondral tissue regeneration with dual functional units, Bioact. Mater. 27 (2023) 200–215, https://doi.org/10.1016/j.bioactmat.2023.04.002.
[70] J. Liu, Y.S. Kim, C.E. Richardson, A. Tom, C. Ramakrishnan, F. Birey, T. Katsumata, S.C. Chen, C. Wang, X. Wang, L.M. Joubert, Y.W. Jiang, H.L. Wang, L.E. Fenno, J.B. H. Tok, S.P. Pasca, K. Shen, Z.A. Bao, K. Deisseroth, Genetically targeted chemical assembly of functional materials in living cells, tissues, and animals, Science 367 (2020) 1372–1376, https://doi.org/10.1126/science.aay4866.
[71] M.A. Gebbie, W. Wei, A.M. Schrader, T.R. Cristiani, H.A. Dobbs, M. Idso, B. F. Chmelka, J.H. Waite, J.N. Israelachvili, Tuning underwater adhesion with cation–π interactions, Nat. Chem. 9 (2017) 473–479, https://doi.org/10.1038/nchem.2720.
[72] D.A. Dougherty, The cation– π interaction, Acc. Chem. Res. 46 (2013) 885–893, https://doi.org/10.1021/ar300265y.
[73] B.P. Dimitrijević, S.Z. Borozan, S.D. Stojanović, π–π and cation–π interactions in protein–porphyrin complex crystal structures, RSC Adv. 2 (2012) 12963–12972, https://doi.org/10.1039/C2RA21937A.
[74] X. Xiao, H. Chen, X. Dong, D. Ren, Q. Deng, D. Wang, W. Tian, A double cation–π-driven strategy enabling two-dimensional supramolecular polymers as efficient catalyst carriers, Angew. Chem. Int. Ed. 59 (2020) 9534–9541, https://doi.org/10.1002/ange.202000255.
[75] S. Hong, Y. Wang, S.Y. Park, H. Lee, Progressive fuzzy cation-π assembly of biological catecholamines, Sci. Adv. 4 (2018) eaat7457, https://doi.org/10.1126/sciadv.aat7457.
[76] A.Y. Clark, K.E. Martin, J.R. García, C.T. Johnson, H.S. Theriault, W.M. Han, D. W. Zhou, E.A. Botchwey, A.J. García, Integrin-specific hydrogels modulate transplanted human bone marrow-derived mesenchymal stem cell survival, engraftment, and reparative activities, Nat. Commun. 11 (2020) 1–14, https://doi.org/10.1038/s41467-019-14000-9.
[77] J. Baek, P.A. Lopez, S. Lee, T.-S. Kim, S. Kumar, D.V. Schaffer, Egr1 is a 3D matrix–specific mediator of mechanosensitive stem cell lineage commitment, Sci. Adv. 8 (2022), eabm4646, https://doi.org/10.1126/sciadv.abm4646.
[78] S.A. Maynard, A. Gelmi, S.C. Skaalure, I.J. Pence, C. Lee-Reeves, J.E. Sero, T. E. Whittaker, M.M. Stevens, Nanoscale molecular quantification of stem cell–hydrogel interactions, ACS Nano 14 (2020) 17321–17332, https://doi.org/10.1021/acsnano.0c07428.
[79] K. Gwon, H.J. Hong, A.M. Gonzalez-Suarez, M.Q. Slama, D. Choi, J. Hong, H. Baskaran, G. Stybayeva, Q.P. Peterson, A. Revzin, Bioactive hydrogel microcapsules for guiding stem cell fate decisions by release and reloading of growth factors, Bioact. Mater. 15 (2022) 1–14, https://doi.org/10.1016/j.bioactmat.2021.12.008.
[80] M. Ermis, N. Falcone, N. Roberto de Barros, M. Mecwan, R. Haghniaz, A. Choroomi, M. Monirizad, Y. Lee, J. Song, H.J. Cho, Y. Zhu, H. Kang, M. R. Dokmeci, A. Khademhosseini, J. Lee, H.J. Kim, Tunable hybrid hydrogels with multicellular spheroids for modeling desmoplastic pancreatic cancer, Bioact. Mater. 25 (2023) 360–373, https://doi.org/10.1016/j.bioactmat.2023.02.005.
[81] S. Han, R. Deng, X. Xie, X. Liu, Enhancing luminescence in lanthanide-doped upconversion nanoparticles, Angew. Chem. Int. Ed. 53 (2014) 11702–11715, https://doi.org/10.1002/anie.201403408.
[82] M. Rafieian-Kopaei, A. Baradaran, M. Rafieian, Plants antioxidants: from laboratory to clinic, J. Nephropathol. 2 (2013), https://doi.org/10.12860/JNP.2013.26.
[83] M.A. Hope, T. Nakamura, P. Ahlawat, A. Mishra, M. Cordova, F. Jahanbakhshi, M. Mladenović, R. Runjhun, L. Merten, A. Hinderhofer, Nanoscale phase segregation in supramolecular π-templating for hybrid perovskite photovoltaics from NMR crystallography, J. Am. Chem. Soc. 143 (2021) 1529–1538, https://doi.org/10.1021/jacs.0c11563.
[84] B. Sun, Y. Kim, Y. Wang, H. Wang, J. Kim, X. Liu, M. Lee, Homochiral porous nanosheets for enantiomer sieving, Nat. Mater. 17 (2018) 599–604, https://doi.org/10.1038/s41563-018-0107-4.
[85] N. Lardon, L. Wang, A. Tschanz, P. Hoess, M. Tran, E. D'Este, J. Ries, K. Johnsson, Systematic tuning of rhodamine spirocyclization for super-resolution microscopy, J. Am. Chem. Soc. 143 (2021) 14592–14600, https://doi.org/10.1021/jacs.1c05004.
[86] B. Hua, K.Y. Han, R. Zhou, H. Kim, X. Shi, S.C. Abeysirigunawardena, A. Jain, D. Singh, V. Aggarwal, S.A. Woodson, An improved surface passivation method for single-molecule studies, Nat. Methods 11 (2014) 1233–1236, https://doi.org/10.1038/nmeth.3143.
[87] Z. Zhou, K. Maxeiner, P. Moscariello, S. Xiang, Y. Wu, Y. Ren, C.J. Whitfield, L. Xu, A. Kaltbeitzel, S. Han, In situ assembly of platinum (II)-Metallopeptide nanostructures disrupts energy homeostasis and cellular metabolism, J. Am. Chem. Soc. 144 (2022) 12219–12228, https://doi.org/10.1021/jacs.2c03215.
[88] G. Bae, Y.S. Jeon, M.J. Ko, Y. Kim, S.-B. Han, R. Thangam, W. Kim, H.J. Jung, S. Lee, H. Choi, S. Min, H. Hong, S. Park, S.Y. Kim, K.D. Patel, N. Li, J.E. Shin, B. C. Park, H.S. Park, J.H. Moon, Y.J. Kim, U.K. Sukumar, J.-J. Song, S.Y. Kim, S.-H. Yu, Y.C. Kang, P. Steve, S.M. Han, D.-H. Kim, K.-B. Lee, Q. Wei, L. Bian, R. Paulmurugan, Y.K. Kim, H. Kang, Immunoregulation of macrophages by controlling winding and unwinding of nanohelical ligands, Adv. Funct. Mater. 31 (2021), 2103409, https://doi.org/10.1002/adfm.202103409.
[89] W. Zhao, L. Hanson, H.-Y. Lou, M. Akamatsu, P.D. Chowdary, F. Santoro, J. R. Marks, A. Grassart, D.G. Drubin, Y. Cui, Nanoscale manipulation of membrane curvature for probing endocytosis in live cells, Nat. Nanotechnol. 12 (2017) 750, https://doi.org/10.1038/nnano.2017.98.
[90] S.E. Gratton, P.A. Ropp, P.D. Pohlhaus, J.C. Luft, V.J. Madden, M.E. Napier, J. M. DeSimone, The effect of particle design on cellular internalization pathways, Proc. Natl. Acad. Sci. USA 105 (2008) 11613–11618, https://doi.org/10.1073/pnas.0801763105.
[91] V.K. Switacz, S.K. Wypysek, R. Degen, J.J. Crassous, M. Spehr, W. Richtering, Influence of size and cross-linking density of microgels on cellular uptake and uptake kinetics, Biomacromolecules 21 (2020) 4532–4544, https://doi.org/10.1021/acs.biomac.0c00478.
[92] Y. Zhang, Y. Zhang, G. Song, Y. He, X. Zhang, Y. Liu, H. Ju, A DNA–azobenzene nanopump fueled by upconversion luminescence for controllable intracellular drug release, Angew. Chem. Int. Ed. 131 (2019) 18375–18379, https://doi.org/10.1002/anie.201909870.
[93] L. Xiong, T. Yang, Y. Yang, C. Xu, F. Li, Long-term in vivo biodistribution imaging and toxicity of polyacrylic acid-coated upconversion nanophosphors, Biomaterials 31 (2010) 7078–7085, https://doi.org/10.1016/j.biomaterials.2010.05.065.
[94] H. Oliveira, A. Bednarkiewicz, A. Falk, E. Fröhlich, D. Lisjak, A. Prina-Mello, S. Resch, C. Schimpel, I.V. Vrček, E. Wysokińska, Critical considerations on the clinical translation of upconversion nanoparticles (UCNPs): recommendations from the European upconversion network (COST Action CM1403), Adv. Healthcare Mater. 8 (2019), 1801233, https://doi.org/10.1002/adhm.201801233.